A&A manuscript no.
(will be inserted by hand later)

Your thesaurus codes are:
07(02.12.1; 02.12.3; 02.18.7; 08.05.1; 08.13.2; 08.18.1)

ASTRONOMY
AND
ASTROPHYSICS
13.12.1995

H_α Line Formation in Hot Star Winds – The Influence of Rotation

P. Petrenz and J. Puls

Institut für Astronomie und Astrophysik der Universität München, Scheinerstr. 1, D-81679 München, Germany

Received; accepted

Abstract. We investigate the influence of stellar rotation on the H_α line formation in O-star winds. The 2-D wind model used is based on the kinematical approach by Bjorkman & Cassinelli (1993, BC), adapted to the parameter space considered in this paper. We discuss only those cases where the rotational rates are well below those that would induce an onset of disk formation.

The influence of gravity darkening on the line formation is shown to be negligible, as long as appropriate *averaged* photospheric parameters (which then are a function of the rotational rate) are used. The distortion of the stellar radius from sphericity can likewise be neglected in most cases.

Our investigations show that the H_α line formation is strongly affected by two processes which we call the *resonance zone* and the ρ^2*-effect*. The former process diminishes the emission near the line core and enhances the emission in both wings due to a twist in the resonance zones induced by differential rotation. The latter process leads to an increase in the overall emission due to the density contrast between the polar and the equatorial zones caused by the deflection of material towards the equator in the BC-model.

We compare the line profiles from our 2-D models with those resulting from the conventional 1-D approach, as a function of absolute or projected rotational velocity, and inclination angle and mass-loss rate.

It is shown that in *all* cases independent of inclination angle and rotational rate, the 1-D method – for a given mass-loss rate – yields the smallest wind emission. This in turn means that all mass-loss rates presently derived from H_α are *overestimated*, with typical errors of $20\ldots30\%$. The *maximum* error introduced by this simplified approach is of the order $50\ldots70\,\%$ for O-Supergiants and occurs for stars with *small* $v_{\rm rot}\sin i$ and observed nearly pole on.

Moreover, our theoretical line *shapes* show a number of features actually found in the observations of rapidly rotating stars.

Finally, the specific influence of the rotational rate and inclination angle which both, *independently* modify the profiles in a distinctive way may provide us with a method for the determination of $\sin i$ from H_α line fits (in connection with the analysis of other spectral regions) in future investigations.

Send offprint requests to: P. Petrenz

Key words: Line: formation – Line: profiles – Radiative transfer – Stars: early type – Stars: mass-loss – Stars: rotation

1. Introduction

In recent years, considerable progress has been made in both the theoretical modelling and the quantitative spectroscopy of radiation driven winds of hot stars (e.g., Pauldrach et al. 1994, Schaerer & Schmutz 1994, Puls et al. 1993 and references therein). As a result of these advances, stellar winds can now be used as tools for astrophysical investigations; in particular, they provide a powerful new method for extragalactic distance determinations. From a theoretical point, this is possible because the stellar mass-loss rate $\dot{M}$ and the terminal velocity of the wind v_∞ can be expressed as functions of stellar parameters (cf. Kudritzki et al. 1992). However, the formulation of these functions requires very detailed and time-consuming calculations and may – with respect to quantitative results – suffer from certain assumptions and approximations present in the models.

Nevertheless, the wind-momentum luminosity relation (WLR) between the modified wind momentum rate, $\dot{M} v_\infty R_*^{\frac{1}{2}}$, and the stellar luminosity, L, which was recently established on a completely *empirical* basis (Kudritzki et al. 1995), is extremely promising, especially since it appears to be valid for luminous stars of all spectral types between O and A (cf. also McCarthy et al. 1995).

This relation, which mainly depends on stellar metallicity, has also been understood from a theoretical point of view (Puls et al. 1995, hereafter Pu95), and one of the primary goals in our group is to calibrate this relation for different metallicities.

In order to use this relation, a reliable value for the "observed" mass-loss must be available. This in turn demands a detailed knowledge of the conditions in the stellar wind. In contrast, most of the other required quantities (especially the metallicity) follow either from a photospheric analysis (e.g., from the iron group lines, cf. Becker & Butler 1995a/92/95b for Fe IV/V/VI, further work is in progress) or – with respect to v_∞ – from a more or less simple analysis of UV resonance lines (e.g., Groenewegen & Lamers 1989, Haser et al. 1994) or optical metal lines (in cooler stars).

The mass-loss rate itself can be determined by two different, well-established methods: Firstly, one can investigate the bound-free and free-free excess of the IR and radio continuum (Wright & Barlow 1975, Panagia & Felli 1975, Lamers & Waters 1984) and, secondly, one can analyze the H_α line (Leitherer 1988a, Pu95).

The IR-/radio excess has been used, e.g., by Barlow & Cohen (1977), Lamers (1981), Abbott et al. (1984), Bieging et al. (1989) and Leitherer & Robert (1991). For extragalactic objects, however, one is restricted to the second method because of the extremely low flux densities in the radio and IR range. So far, this method has been applied for the mass-loss determinations of OB-stars (Leitherer 1988a/b, Scuderi et al. 1992, Lamers & Leitherer 1993 (LL93), Pu95) and for A-type Hypergiants (Stahl et al. 1991).

However, all the above investigations suffer from two approximations, which may have severe consequences for quantitative interpretations: The influence of *stellar rotation* both on the radiative transfer and on the underlying hydrodynamics of the stellar wind has been taken into account in an only very approximate way, if at all.

Influence of stellar rotation on the radiative transfer. The conventional method of incorporating stellar rotation in the H_α line formation process presumes that the major part of the H_α emission originates in the lowest wind part, i.e., the emitting material is assumed to co-rotate with the stellar surface. Hence, the usual procedure is either to neglect rotation completely (if methods based on equivalent widths are used) or to calculate the emission for a non-rotating, spherically symmetric wind and subsequently to convolve the emergent profile with a rotation profile of width $v_{\rm rot} \sin i$, which is determined from photospheric lines.

The latter approach, however, is very questionable, since the *differential* rotational velocity $v_{\rm rot}(r)$ is inversely proportional to the distance from the star, r, and consequently decreases rapidly in the region close to the star. Thus, for larger distances the wind material does not co-rotate with the stellar surface, and the emitted radiation experiences a smaller broadening than given by the photospheric value. Accordingly, one has at least in principle to account for the deformation of the particle streamlines caused by the differential rotation of the wind. Up to now, this has been done only for the H_α emission in Be-star envelopes (Hummel 1992) and for the scattering dominated UV P Cygni lines in hot star winds, which are formed throughout the *entire* atmosphere and hence are only mildly affected by this process (Mazzali 1990, Bjorkman et al. 1994; see also Shlosman & Vitello 1993, for the UV line formation in winds from accretion disks of CVs). The effect on the H_α emission in OB star winds, however, has not been investigated so far.

The influence of stellar rotation on the hydrodynamics of the wind was first estimated by Friend & Abbott (1986, hereafter FA) and Pauldrach, Puls & Kudritzki (1986, hereafter PPK), who solved the fluid equations including centrifugal forces only in the equatorial plane, thus neglecting the lateral dependence of $v_{\rm rot}$. In so doing, they considered the "global" impact of differential rotation, where the actual mass-loss rate lies in between the equatorial and the polar value.

This approximation was dropped by Bjorkman & Cassinelli (1993, hereafter BC). They solved the hydrodynamical equations (including lateral terms) in the supersonic part of the wind analytically and provided simple expressions for the velocity field and density structure. As a result, they found the density to increase from the poles towards the equatorial plane (at constant r) and this density contrast to become enhanced with r. In the most extreme situations with $\Omega \gtrsim 0.8 \ldots 0.9$ (for O-stars) or $\Omega \gtrsim 0.5$ (for B-stars), an equatorial disk should develop ($\Omega = v_{\rm rot}/v_{\rm crit}$ with $v_{\rm rot}$ the equatorial value and $v_{\rm crit}$ the "breakup" velocity). Even this prediction has been confirmed by detailed numerical simulations (Owocki et al. 1994), although their results differed in some respects from those by BC. Thus the BC model, though very simple, seems to be a reliable way of simulating the density structure of rotating O-star winds, where the physical conditions are less extreme.

Finally, the inclusion of rotation in the derivation of mass-loss rates may also resolve a problem that arises if one carefully compares the values obtained from H_α- and radio excess methods, which both depend on processes proportional to the square of the density and thus should result in compatible values. Although on average the two values are in good agreement (cf. LL93, Pu95, Najarro & Puls 1996, in prep.), for some stars a distinct discrepancy larger than the error-bars remains. E.g., for the often analyzed object ζ Pup (O4If) the radio method yields $\dot M$(Radio) = $2.4 \ldots 3.1 \times 10^{-6} M_\odot {\rm yr}^{-1}$ (first value from LL93, second from Najarro & Puls, combined IR and radio), whereas the H_α method gives $\dot M(H_\alpha) = 5.0 \ldots 5.9 \times 10^{-6} M_\odot {\rm yr}^{-1}$, if the same set of stellar parameters is used (Pu95).

However, ζ Pup is quite a fast rotator with a projected rotational velocity $v_{\rm rot} \sin i = 220\,{\rm km\,s}^{-1}$, which implies that it is observed more or less equator-on (see also Howarth et al. 1995). The H_α emission originates from lower wind layers, typically between $1 \ldots 1.5$ stellar radii, whereas the radio emission is generated in the outer part of the wind ($\gtrsim 50 \ldots 100$ stellar radii). If one additionally considers that the density contrast between the pole and the equator increases with radius (see above), then one should observe a rather broad ring around the star in H_α and a radio photosphere which is compressed towards the equatorial plane. Thus, it is possible that the radio emission would provide a lower mass-loss rate than deduced from the H_α line synthesis, if conventional methods neglecting rotation are applied.

The consequences of the other extreme, when a rapid rotator is observed pole-on, are more difficult to estimate. As will be shown in this paper, in any case the H_α mass-loss rate derived by neglecting the influence of rotation will be larger than it would be if the same star is observed equator-on. With respect to a comparison with conventionally derived radio mass-loss rates, it may be possible that the latter are larger, since the projected H_α emitting region is not as enlarged as the projected area of the radio photosphere. This scenario may actually occur: Pu95 found a number of stars with low $v_{\mathrm{rot}} \sin i$ *and* $\dot{M}(\mathrm{H}_\alpha) < \dot{M}$(Radio), which suggests that these stars have a large v_{rot}. However, detailed calculations including a 2-D treatment of continua seen pole-on have to be made before a final conclusion can be drawn.

In the present paper, we will investigate the principle effects of stellar rotation on the H_α line formation in stationary winds. For a typical O-Supergiant wind, we will successively refine the model to include the effects of differential rotation, 2-D density structure and gravity darkening. Since a precise 2-D hydrodynamical description of the wind is beyond the scope of this paper, we will make use of the comparatively simple BC model. In particular, we will investigate the extent to which the determination of the mass-loss rate is affected by differential rotation and estimate the error introduced by the conventional 1-D analysis.

The rest of the paper is organized as follows: In section 2 we present our model of the H_α transition, and in section 3 we investigate the properties of different models for the stellar wind. The line formation process and the influence of differential rotation are described in section 4. In section 5 we study basic effects on line profiles and discuss the consequences for the determination of $\dot{M}$ from H_α. A discussion of the results and the future perspectives are finally given in section 6.

2. The H_α line

2.1. Assumptions and approximations for the radiative transfer

In the treatment of the H_α line formation, we will assume the following simplifying approximations:

- Since we are primarily interested in pure H_α line formation, we will neglect the HeII blend at 6560 Å. This assumption holds for stars with a low He abundance Y_{He}, but is problematic in the case of higher Y_{He} because of the increasing contribution of the He blend to the line- and equivalent width (absolute value). In particular, the large values of the NLTE departure coefficient of the upper level lead to an enhanced emission (with respect to LTE) which might even compensate for the lower abundance (with respect to hydrogen) and necessitates the inclusion of this blend in quantitative analyses (cf. Pu95). However, as a first step and in order to disentangle the effects of stellar rotation in a clear way, this paper deals exclusively with the hydrogen component. Obviously, this approximation has to be dropped in the final application.
- We consider an optically thin continuum in the wind at the frequencies of the Balmer lines, which is a good approximation for O-star winds. The photospheric continua and corresponding absorption profiles are taken from an interpolation on a grid of plane-parallel NLTE model fluxes (Herrero, priv. comm.), where the He-component has been artificially removed.
- The radiative transfer itself is calculated in the generalized 3-D Sobolev approximation (Rybicki & Hummer 1978), since in this way the computation time is significantly reduced and, moreover, the different effects due to the velocity field and density can be disentangled easily. This approach should not introduce substantial errors, since the lower boundary of our wind models is given by the sonic point (see §3.5). Evidently, the use of a consistent hydrodynamical structure with a lower boundary at much smaller velocities would require the solution of the "exact" formal integral.

2.2. Optical depth and source function

In the Sobolev approximation, the optical depth τ in direction $\boldsymbol{n}$ at location $\boldsymbol{r}$ is given by

$$\tau(\boldsymbol{r}, \boldsymbol{n}) = \frac{C\,\rho^2(\boldsymbol{r})}{|\mathrm{d}(\boldsymbol{n}\boldsymbol{v})/\mathrm{d}\boldsymbol{n}|}, \tag{1}$$

where ρ denotes the density of the wind, and $|\mathrm{d}(\boldsymbol{n}\boldsymbol{v})/\mathrm{d}\boldsymbol{n}|$ is the directional derivative of the velocity $\boldsymbol{v}(\boldsymbol{r})$ in direction $\boldsymbol{n}$. In C we have mainly absorbed the physical parameters of the H_α ($3 \rightarrow 2$) transition. It can be easily derived from the definition of the Sobolev optical depth (e.g., Sobolev 1957; Castor 1970) and by applying the Saha-Boltzmann equation, however allowing for departures from LTE (e.g., Leitherer 1988):

$$\begin{aligned} C \;&=\; 6.60 \cdot 10^{20}\, T_{\mathrm{e}}^{-3/2} \times \frac{1 + Y_{\mathrm{He}} I_{\mathrm{He}}}{(1 + 4Y_{\mathrm{He}})^2} \\ &\times \left[b_2(r) \exp\left(\frac{3.945}{T_{\mathrm{e}}}\right) - b_3(r) \exp\left(\frac{1.753}{T_{\mathrm{e}}}\right) \right]. \end{aligned}$$

Here T_{e} is the electron temperature in 10^4 K, Y_{He} the He abundance $n_{\mathrm{He}}/n_{\mathrm{H}}$ and I_{He} the average number of free electrons provided per He atom (assumed to be 2 throughout this paper).

The quantities b_2 and b_3 denote the non-LTE departure coefficients, as obtained by an analysis of the occupation number stratification of the upper and lower levels using "unified model atmospheres" (Gabler et al. 1989) and parameterized as function of radial velocity v_r (see Pu95, Eq. 45). The departure coefficients refer to a renormalized constant electron temperature $T_{\mathrm{e}} = 0.75\, T_{\mathrm{eff}}$.

Strictly speaking, this parameterization as function of $v_r(r)$ applies only for the case of purely radially expanding winds. However, we will use it also for the cases including differential rotation and 2-D density depending both on distance from the star and on stellar latitude, since at present the correct 2-D parameterization is not known and the deviations from unity are anyway small (provided, that we neglect the He blend).

For our first model, we concentrate on the effects of differential rotation alone, and leave the density at its 1-D value (cf. §3.3). By means of the equation of continuity

$$\dot{M} = 4\pi r^2 v_r \rho(r) \tag{2}$$

(where v_r is the radial velocity), we obtain

$$\tau(\boldsymbol{r}, \boldsymbol{n}) = \frac{A'(r)}{r^4\, v_r(r)^2\, |\mathrm{d}(\boldsymbol{n}\boldsymbol{v})/\mathrm{d}\boldsymbol{n}|}, \tag{3}$$

with $A^{'}(r) = C\,(\dot{M}/4\pi)^2$. To give an impression of the order of magnitude of τ, we note that $A^{'}/(v_\infty^3 {R_*}^3)$ is equivalent to the quantity $A(r)$ given in Pu95 (see their Eq. 3) and ranges from 10^{-1} to 10^{-7}, which implies that bulk of the wind is optically thin in H_α.)

Using the above departure coefficients, the line source function S_l is finally given by

$$S_\mathrm{l} = \frac{1.404 \cdot 10^{-3}}{\frac{b_2(r)}{b_3(r)}\, e^{(2.192/T_\mathrm{e})} - 1}. \quad (4)$$

3. The stellar wind

In this section we discuss the different models we adopt for differentially rotating stellar winds, with special emphasis on the extent to which these models differ from conventional models of non-rotating winds. In successive steps we will drop the assumptions of

1. 1-D spherically symmetric radiative transfer
2. 1-D density stratification in the wind
3. constant photospheric gravity at all latitudes

and investigate the consequences for the wind properties.

3.1. Simplifying assumptions

For all models we will adopt the following simplifications:

– *stationary* and *smooth flow* of the wind (i.e., no "clumps" and no shocks)
– a *spherically symmetric* star.

Since the H_α opacity/emissivity scales with the square of the density, the neglect of a possible clumpiness in the wind can have severe consequences, as has been discussed by Abbott et al. (1981) and Lamers & Waters (1984a); see also Puls et al. (1993). However, if we account for the fact that the major contribution to the H_α emission in O-star winds arises from the lower regions (typically from $1.0 \ldots 1.5$ stellar radii) and most recent hydrodynamical simulations have shown pronounced wind inhomogeneities only above these layers (see Owocki 1994), this neglect most probably will not induce any severe and systematic errors into the mass loss determination. (For a more thorough discussion on the validity of the first approximation we refer the reader to Pu95.)

With the second approximation, we neglect the distortion of the stellar surface due to stellar rotation (see Collins 1963). However, in the course of our investigations with respect to gravity darkening (§3.6), this assumption will be relaxed in some respects.

3.2. The velocity field

The velocity field at location $\boldsymbol{r}$ is given by

$$\boldsymbol{v}(\boldsymbol{r}) = v_r(\boldsymbol{r})\boldsymbol{e}_r(\boldsymbol{r}) + v_\Phi(\boldsymbol{r})\boldsymbol{e}_\Phi(\boldsymbol{r}) + v_\Theta(\boldsymbol{r})\boldsymbol{e}_\Theta(\boldsymbol{r})\,, \quad (5)$$

where (r, Θ, Φ) denote spherical polar coordinates (Θ is measured from the rotational pole) and $\boldsymbol{e}_r, \boldsymbol{e}_\Theta, \boldsymbol{e}_\Phi$ the unit vectors in radial, polar and azimuthal direction.

3.3. Models with spherically symmetric density stratification

In our first step to disentangle the different effects of velocity and density structure, we will assume a 1-D density stratification $\rho(\boldsymbol{r}) = \rho(r)$, which only depends on the radial coordinate and is given by Eq.(2). In contrast to the conventional H_α-synthesis, however, we will correctly account for the influence of differential rotation via the velocity field and its directional derivative (see §5.2).

In this case, the radial component v_r is given by the usual β-velocity field

$$v_r(r) = v_\infty \left(1 - \frac{b}{x}\right)^\beta, \quad b = 1 - \left(\frac{v_\mathrm{min}}{v_\infty}\right)^{1/\beta} \quad (6)$$

with $x \equiv r/R_*$ the normalized distance from the stellar centre, v_min the minimum and v_∞ the terminal wind velocity. β controls the shape of the velocity field and ranges from 0.7 ... 1.3 for typical O-star winds (cf. Groenewegen & Lamers 1989, Pu95). We will use $\beta = 1$ as a representative value in our investigations.

The azimuthal velocity component v_Φ is due to the stellar rotation. With the assumption of conservation of angular momentum, we have

$$v_\Phi(r, \Theta) = v_\mathrm{rot}\,\frac{\sin\Theta}{x}, \quad (7)$$

with v_rot the equatorial rotational velocity at the stellar surface.

The polar component v_Θ is set to zero,

$$v_\Theta = 0,$$

since in this first model we will investigate the influence of the differential rotation exclusively.

In this description then, the velocity field is symmetric about the rotational axis and the equatorial plane in the stellar reference frame.

3.4. Models with 2-D density stratification

Since the optical depth is proportional to the square of the density, a correct treatment of the density stratification in the whole wind is essential for the line formation process. As already mentioned in §1, BC presented a wind model for rapidly rotating early type stars that predicts a 2-D density stratification $\rho(r, \Theta)$. A thorough discussion of this model is given by BC, and we will only briefly describe the basic features and then discuss the resulting wind properties in the case of typical O-stars.

As a basic assumption, BC use the supersonic approximation, i.e., pressure terms are neglected when calculating the particle trajectories. Thus, a parcel of wind material behaves like a non-interacting free Newtonian particle, and the only forces to be considered are radiation pressure, centrifugal acceleration and gravity. Furthermore, the boundary conditions at all latitudes are set by $r_i = r_s \approx R_*$, with r_s the sonic point, i.e., the rotational distortion of the stellar surface is neglected.

In our further considerations, we will use the same geometry as BC, which is shown in Fig. 1. Θ_0 is the initial "co-latitude"

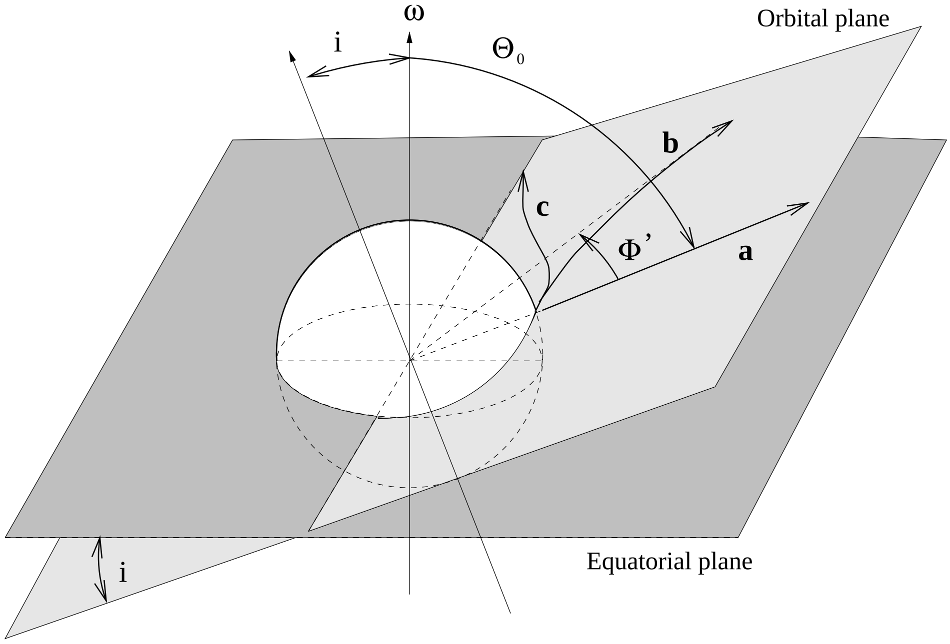

Fig. 1. Geometry of the WCD (wind compressed disk)-model by Bjorkman & Cassinelli. The streamlines originate at polar angle Θ_0. Their orbital plane is tilted relative to the equatorial plane by an angle $i = \pi/2 - \Theta_0$. Φ' denotes the azimuthal angle in the orbital plane. The streamline labeled (a) denotes the case of zero rotational velocity, whereas curve (c) describes the trajectory in the case of extreme rotation. In this case the streamline crosses the equatorial plane at $\Phi' = \pi/2$. Streamline (b) corresponds to the case of moderate rotation considered here.

of the particle at the stellar surface and Φ' the azimuthal angle in the orbital plane, to which the particle motion is confined.

As shown by BC, with increasing rotational rate the trajectories develop from curve (a) ($v_{\rm rot} = 0$) to (b) and (c) (where, in the case of O-stars, $v_{\rm rot}$ is near the breakup velocity). This evolution is caused by the combination of radiation pressure, centrifugal force and gravitation and leads in the case of non-vanishing rotation to a deflection of the particles towards the equatorial plane, which is equivalent to a polar velocity component v_Θ. Consequently, a density concentration from pole to equator is formed.

As pointed out by BC, for *rapid* rotators this deflection becomes extremely strong and causes the wind material originating at near-equator latitudes to collide with the material from the other hemisphere at the equatorial plane. This leads to a density contrast between equator and pole up to 10^3 (BC, Eq. 51), i.e., a "disk" forms. In this case, the pressure terms dominate in the equatorial plane, and the supersonic approximation breaks down in this region.

Since we are interested in O-stars, where the onset of disk formation is estimated to occur at $v_{\rm rot} \gtrsim 0.9\, v_{\rm crit}$ (see BC, Tab. 2)), i.e., $v_{\rm rot} \gtrsim 450$ km s^{-1}, the approximate solutions given in the next section should be reliable for $v_{\rm rot} \lesssim 300$ km s^{-1}, at least for qualitative investigations (cf. also Cassinelli et al. 1995, who applied the original BC-model to the compression of Wolf-Rayet winds in the *non disk formation case*, referring to it as the wind compression zone (WCZ) model.).

3.4.1. Velocity field

BC provide a semi-analytical solution for the velocity field $\boldsymbol{v}(r,\Theta)$ and the density stratification $\rho(r,\Theta)$ (see their Eqs. 20/22). Compared with their radial velocity law $v_r(r) = v_\infty(\Theta_0)\,(1-1/x)^\beta$, we use a somewhat different expression

$$v_r(r,\Theta_0) = v_\infty(\Theta_0) \left(1 - \frac{b}{x}\right)^\beta, \qquad \text{with} \tag{8}$$

$$b = 1 - \left(\frac{v_{\rm min}}{v_\infty(\Theta_0)}\right)^{1/\beta}, \tag{9}$$

$$v_\infty(\Theta_0) = \zeta\, v_{\rm esc} \left(1 - \sin\Theta_0 \frac{v_{\rm rot}}{v_{\rm crit}}\right)^\gamma. \tag{10}$$

Here $v_{\rm esc}$ is the photospheric escape velocity $v_{\rm esc} = \sqrt{2}\, v_{\rm crit}$, $v_{\rm crit}$ is the break-up velocity, $v_{\rm crit} = \sqrt{GM_*(1-\Gamma)/R_*}$, $\Gamma = \sigma_e L_*/(4\pi c\, GM_*)$ accounts for the acceleration due to Thomson scattering, and M_* is the stellar mass. In this definition of $v_{\rm crit}$, we have neglected the rotational distortion of the stellar surface (see above).

The parameter γ is determined by fitting results obtained from "exact" hydrodynamical calculations; from FA, it has been set to $\gamma = 0.35$. As outlined above, we will use an exponent $\beta = 1$ (BC: $\beta = 0.8$) since our models should allow also for winds with a moderate radial velocity gradient valid for O-type Supergiants (cf. Pu95). Finally, ζ is given by (cf. FA, Eq. 8)

$\zeta = v_\infty/v_{\rm esc} \approx (v_{\rm esc}/1\,000\,{\rm km\,s^{-1}})^{0.2}\,2.2\alpha/(1-\alpha)$ with force multiplier parameter α.

With this parameterization of the radial velocity component, the azimuthal and polar components result in (cf. BC)

$$v_\Phi(r,\Theta) = \frac{v_{\rm rot}}{x}\frac{\sin^2\Theta_0}{\sin\Theta} \tag{11}$$

$$v_\Theta(r,\Theta) = \frac{v_{\rm rot}}{x}\frac{\sin\Theta_0\cos\Theta_0}{\sin\Theta}\sin\Phi', \tag{12}$$

where in our case (cf. Appendix A)

$$\Phi' = \frac{1}{b(1-\beta)}\left\{\left(1-\frac{b}{x}\right)^{1-\beta} - (1-b)^{1-\beta}\right\} \times \frac{\sin\Theta_0 v_{\rm rot}}{v_\infty(\Theta_0)}, \tag{13}$$

and $\Theta_0(r,\Theta)$ can be found by iteratively solving for (cf. BC, Eq. 19)

$$\cos\Theta = \cos\Theta_0\cos\Phi' \tag{14}$$

in parallel with Eq. (13) for Φ'.

3.4.2. Density stratification

For the case of *non-crossing* streamlines (i.e., $\Phi' < \pi/2$), the wind density is given by (BC, Eq. 22)

$$\rho(r,\Theta) = \frac{\dot M(\Theta_0)}{4\pi r^2 v_r\,({\rm d}\mu/{\rm d}\mu_0)}, \tag{15}$$

with $\mu = \cos\Theta$ and $\dot M(\Theta_0)$ the mass flux multiplied by $4\pi R_*^2$

$$\dot M(\Theta_0) = \dot M_{\rm nr}\left(1-\sin\Theta_0\frac{v_{\rm rot}}{v_{\rm crit}}\right)^\xi, \tag{16}$$

where $\xi = -0.43$ and $\dot M_{\rm nr}$ the mass-loss rate of the non-rotating star (see FA). The expression for ${\rm d}\mu/{\rm d}\mu_0$ is derived in Appendix A.

3.5. Model results

In the following section, we will investigate the properties of our modified velocity field and 2-D density structure for a typical O-star wind and compare them with those which would follow from a 1-D spherically symmetric density stratification.

For this purpose, our stellar/wind model is based on the following parameters (close to those obtained for ζ Pup (cf. Pu95))

- $T_{\rm eff}$ = 42 000 K
- $\log g$ = 3.6
- R_* = 19 $R_\odot$
- M_* = 52.5 $M_\odot$
- L_* = 10^6 $L_\odot$
- $v_{\rm esc}$ = 730 km s^{-1}.
- $v_{\rm min} = v_{\rm sound} \approx$ 20 km s^{-1}
- $v_{\infty,\rm pole}$ = 2250 km s^{-1}
- β = 1
- α = 0.6

$v_{\rm sound}$ denotes the isothermal sound speed. Two aspects motivated our choice for $v_{\rm min}$. First, the Sobolev approximation (for hydrogen) breaks down below the sonic point. Secondly, we found from test calculations that for the adopted stellar parameters and a minimum velocity $v_{\rm min} \lesssim 5$ km s^{-1} the onset of disk formation (i.e., $\Phi' \geq \pi/2$) occured already for $v_{\rm rot} \approx 220$ km s^{-1}. This extremely low value, however, seems physically more than questionable, and a correct hydrodynamical 2-D treatment should provide a larger value (cf. also the discussion of this point by Owocki et al. 1994, who came to the same conclusion). Hence and in accordance with BC who assumed $r_i \approx r_s$ as lower boundary, we choose $v_{\rm min} \approx v_{\rm sound}$.

In their investigation of *B-stars*, BC used ζ as a free parameter, since a clear discrepancy between theoretically predicted and observed values of v_∞ occurs for stars in that spectral range with canonical values of α. In our case, however, the observed v_∞ implies a value $\zeta \approx 3.08$, which is compatible with a typical force-multiplier parameter $\alpha \approx 0.6$ (actually, not α but $\alpha - \delta$ plays the crucial role, with f.-m. parameter δ accounting for changes in the ionization structure , cf. Pu95).

At first, we will investigate the behaviour of the different components of the velocity field, v_r, v_Θ and v_Φ. In Fig. 2 (upper panel) we have plotted the radial component $v_r(r,\Theta)$ for different co-latitudes Θ versus radius x, normalized to the 1-D velocity

$$v_{r,1-{\rm D}} \equiv v_{r,\rm pole}(r) = v_{\infty,\rm pole}(1-b/x)^\beta, \tag{17}$$

with $b = 1-(v_{\rm min}/v_{\infty,\rm pole})^{1/\beta}$ and $v_{\infty,\rm pole} = \zeta v_{\rm esc}$.

As can be seen, the radial flow at all latitudes is slower than in the corresponding 1-D model, and in accordance to Eq. (10) this discrepancy is stronger for larger rotational velocities and at larger co-latitudes. Consequently, if we observe the wind "pole-on", the maximum observed velocity will be higher than for a wind seen "equator-on".

Fig. 2 (middle panel) displays the ratio of the azimuthal component $v_\Phi(r,\Theta)$ to $v_r(r,\Theta)$ for different co-latitudes. Close to the star, there is a clear dominance of the rotational terms compared to the radial expansion. The maximum value occurs in the equatorial plane, where $\sin\Theta = \sin\Theta_0 = 1$ (cf. Eq. 11). For larger radii ($x \gtrsim 1.1$), the azimuthal velocity vanishes, since v_Φ is proportional to $1/x$ and the particle streamlines become purely radial. Hence, especially in cases of high inclinations i with large values of projected rotational velocity, the differential rotation will have a substantial impact on the line formation.

The ratio of the polar component $v_\Theta(r,\Theta)$ to $v_r(r,\Theta)$ is plotted in the lower panel of Fig. 2. Near the stellar surface, the particles still have not experienced any deflection towards the equatorial plane, and accordingly v_Θ is zero. With increasing distance, v_Θ grows most strongly for intermediate co-latitudes, where the combination of an orbital plane, that is tilted relative

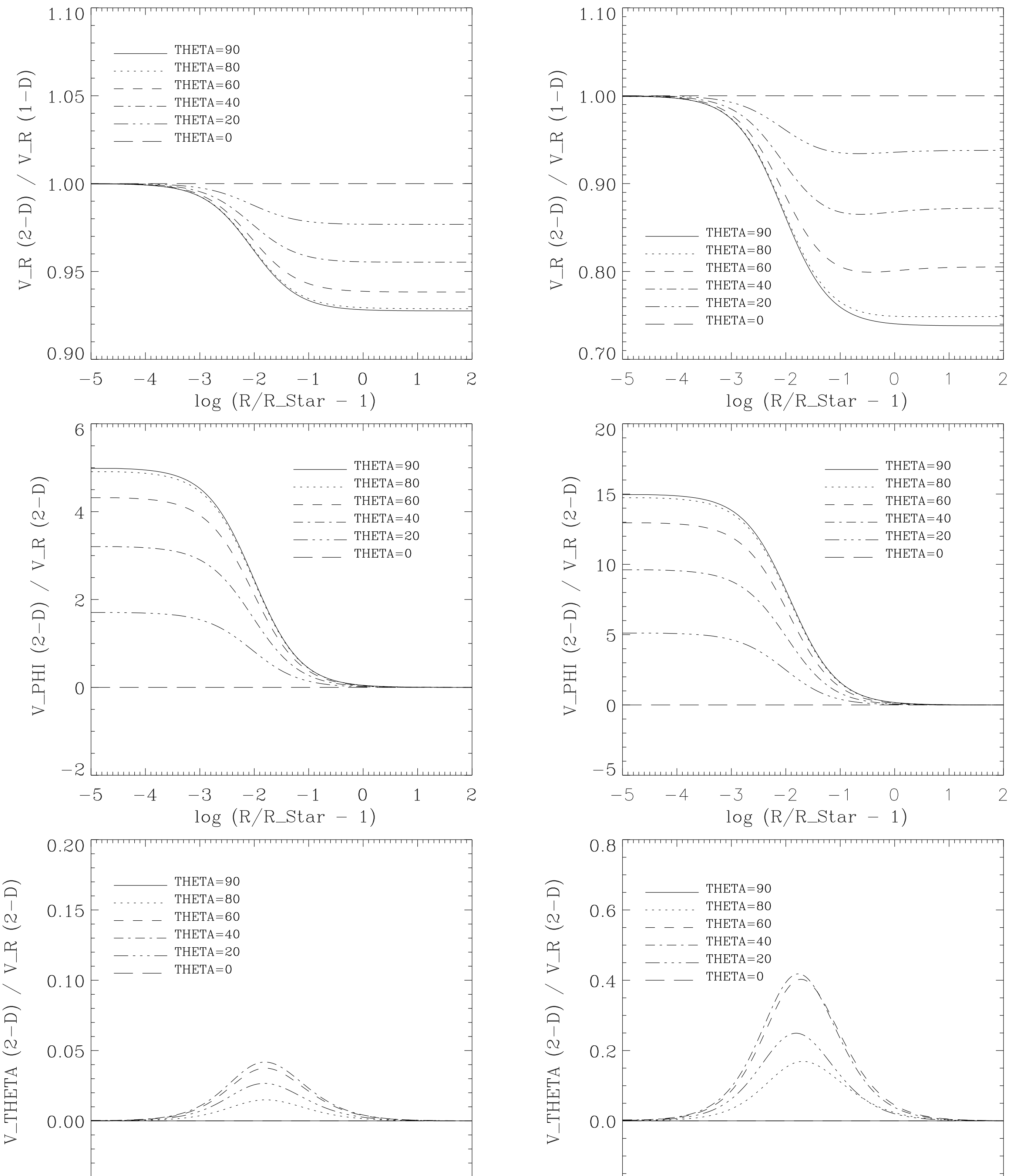

Fig. 2. Velocity components for a stellar wind including rotation vs. distance r from the stellar core for different co-latitudes Θ. Model parameters as in §3.5, stellar radius located at sonic point. Left: $v_{\rm rot}$ = 100 km s^{-1}; right: $v_{\rm rot}$ = 300 km s^{-1}. Upper panel: $v_r(r,\Theta)/v_{r,1-\rm D}(r)$, middle panel: $v_\Phi(r,\Theta)/v_r(r,\Theta)$, lower panel: $v_\Theta(r,\Theta)/v_r(r,\Theta)$.

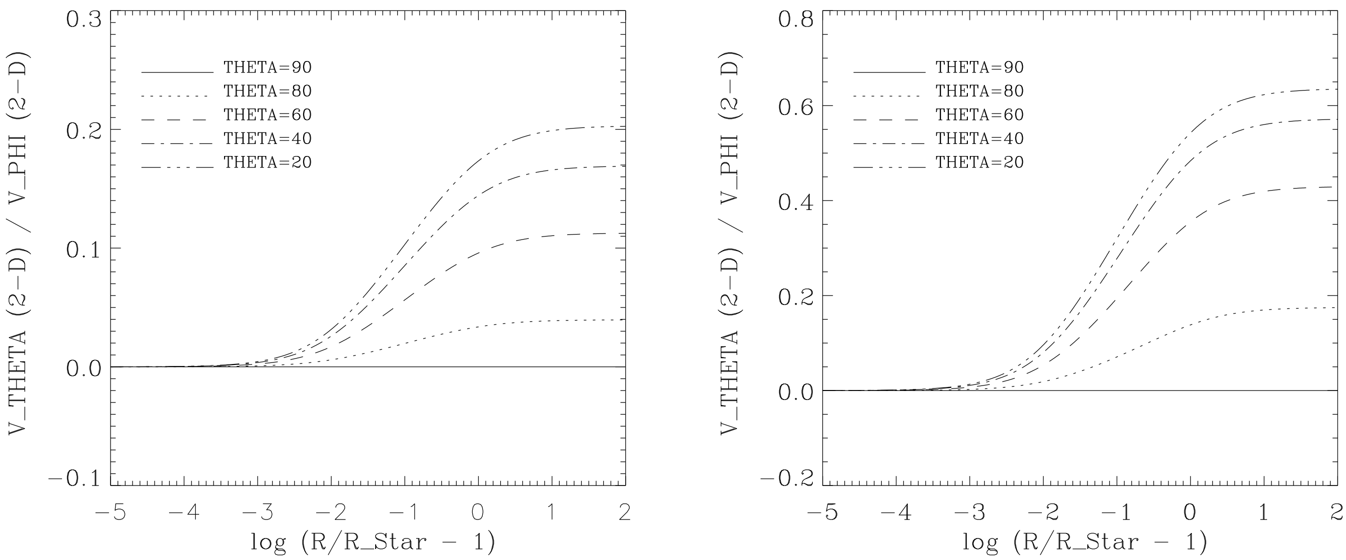

Fig. 2. (continued) The ratio $v_\Theta(r,\Theta)/v_\Phi(r,\Theta)$ vs. r for different co-latitudes Θ. Left: $v_{\rm rot}$ = 100 km s^{-1}; right: $v_{\rm rot}$ = 300 km s^{-1}.

to the equatorial one, and differential rotation is most significant.

v_Θ vanishes both at the poles and in the equatorial plane, in the first case simply because the rotational terms are zero in those regions, and in the second one, because the more the particles are deflected towards the equatorial plane (i.e., the longer they have been moving in their orbital plane) the more radiation pressure dominates the other forces and finally causes a purely radially and outwards directed particle motion.

The (relative) maximum of v_Θ is reached close to the star near $x = 1.01$, where we find values comparable to v_r. For larger radii, v_Θ decreases and finally (almost) vanishes as function of x^{-1}. Since v_Θ is of the same order of magnitude as v_r only very close to the star, its influence on line formation is limited to the line centre (and, moreover, only via an only small emitting/absorbing volume), which is affected anyway by a number of uncertainties such as the actual transition from the quasi-hydrostatic to the wind regime. Hence, we conclude that the impact of v_Θ *on line formation* should be negligible compared to the influence of v_Φ.

This also becomes evident from a direct comparison of the polar and azimuthal velocity components (Fig. 2, last panel). Close to the star ($x \lesssim 1.01 \ldots 1.1$), the polar component v_Θ can be obviously neglected with respect to v_Φ. Significant values are reached only at larger distances from the star, where the maximum of v_Θ/v_Φ converges at $\cot\Theta_0 \sin\Phi'$ (cf. Eqs. 11/12), which itself is largest for low Θ, i.e., in polar regions.

Since in our O-star case the radial velocity v_r clearly dominates both v_Θ and v_Φ for $x \gtrsim 1.1$, neglect of v_Θ compared to v_Φ (as will be done in the following sections) is justified. However, for a detailed treatment of the line core or in cases with a significantly lower terminal velocity (in parallel with high rotational speed, if such a case exists), one may have to consider also the polar component v_Θ both in the velocity field and its directional derivative.

In order to compare the 2-D density stratification $\rho_{2-\rm D} \equiv \rho(r,\Theta)$ with a radially symmetric one $\rho_{1-\rm D} \equiv \rho(r)$, we have to define $\rho(r) \equiv \dot M_{1-\rm D}/(4\pi r^2 v_{r,1-\rm D})$, where $\dot M_{1-\rm D}$ denotes the mass-loss rate of a comparison star with a 1-D density wind being identical to the surface integrated mass flux of the star with the 2-D density wind:

$$\begin{aligned}
\dot M_{1-\rm D} &:= \int_0^{2\pi} R_*^2 \int_0^{\pi} \sin\Theta_0 \, \frac{\dot M(\Theta_0)}{4\pi R_*^2} \, {\rm d}\Theta_0 \, {\rm d}\Phi \\
&= \int_0^{\pi/2} \sin\Theta \left(\frac{{\rm d}\mu}{{\rm d}\mu_0}\right)^{-1} \dot M(\Theta_0) \, {\rm d}\Theta \qquad (18)\\
&=: \int_0^{\pi/2} \sin\Theta \, 4\pi r^2 \rho(r,\Theta) \, v_r(r,\Theta) \, {\rm d}\Theta \quad , \forall r \in [R_*, r_{\rm max}] \, ,
\end{aligned}$$

where we have used Eq. (15) for the third identity. Because the particle streamlines do not cross, the mass flux, integrated over a sphere with radius r, has to be conserved with r. This provides an excellent possibility to test the accuracy of our numerical code. (Parenthetically, we like to comment on the difference between $\dot M_{1-\rm D}$ and $\dot M_{\rm nr}$ from Eq. (16). The mass-loss rate $\dot M_{\rm nr}$ of a non-rotating star changes due to the effects of rotation, leading to an increased surface integrated mass-flux $\dot M_{1-\rm D}$, which will be used throughout the following as *the* mass-loss rate of a 2-D density wind. To give an impression of the change in $\dot M$ as function of rotational rate, for our O-star wind model as above and $\dot M_{1-\rm D} = 6 \cdot 10^{-6} M_\odot {\rm yr}^{-1}$, the corresponding mass-loss rates of a non-rotating star would be $\dot M_{\rm nr} = 5.6 \cdot$

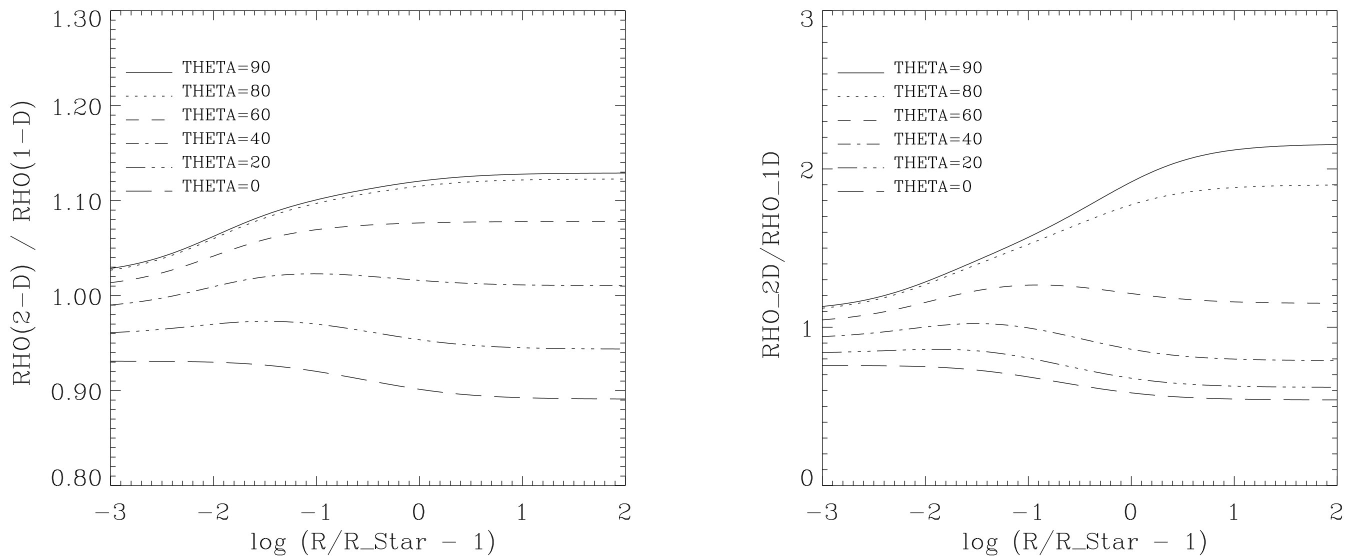

Fig. 3. As Fig. 2, but now for the ratio $\rho(r,\Theta)/\rho_{1-\mathrm{D}}(r)$. Left: $v_{\rm rot}$ = 100 km s^{-1}; right: $v_{\rm rot}$ = 300 km s^{-1}.

$10^{-6}\,M_\odot\,\mathrm{yr}^{-1}$ for $v_{\rm rot}$ = 100 km s^{-1}, $5.1\cdot10^{-6}\,M_\odot\,\mathrm{yr}^{-1}$ ($v_{\rm rot}$ = 200 km s^{-1}) and $4.4\cdot10^{-6}\,M_\odot\,\mathrm{yr}^{-1}$ for $v_{\rm rot}$ = 300 km s^{-1}.)

The results of our calculations are shown in Fig. 3, where we have plotted the ratio between 2-D density $\rho(r,\Theta)$ and 1-D stratification $\rho_{1-\mathrm{D}}$ versus distance x. Already for the case of low $v_{\rm rot}$ = 100 km s^{-1}, we find at constant x a decrease in density around polar latitudes and an enhancement near the equatorial plane. This density contrast between pole and equator becomes more and more pronounced with increasing x, and is extremely significant for a high rotational speed $v_{\rm rot}$ = 300 km s^{-1}, namely $\rho_{\rm equator}/\rho_{\rm pole} \approx 1.5\,(x=1)\ldots4\,(x=r_{\rm max}/R_*)$.

From the constraint of mass-flux conservation, the definition of $\dot M_{1-\mathrm{D}}$ and with reference to Eq. (16), it is obvious that at the pole $\dot M(\Theta_0=0) < \dot M_{1-\mathrm{D}}$ and in the equatorial plane $\dot M(\Theta_0=\pi/2) > \dot M_{1-\mathrm{D}}$. At the stellar surface then, we find from Eq. (A3) that $\mathrm{d}\mu/\mathrm{d}\mu_0 = 1$ ($\Phi'(x=1)=0$). Additionally, we have $v_r(x=1,\Theta) = v_{\rm min} = v_{r,1-\mathrm{D}}$ for all co-latitudes Θ, so that, even at the stellar surface, $\rho(r,\Theta)$ is smaller than $\rho_{1-\mathrm{D}}(r)$ in polar regions and larger than $\rho_{1-\mathrm{D}}(r)$ in equatorial regions.

Although the density contrast is an increasing function of x, it becomes almost constant for large distances from the star ($x \gtrsim 10$), since v_Φ and v_Θ vanish and the streamlines become radial. Interestingly, at intermediate co-latitudes ($\Theta \approx 40°\ldots60°$) the density ratios behave in a strikingly non-monotonic fashion, e.g., for $v_{\rm rot}$ = 300 km s^{-1} and $\Theta = 40°$, $\rho_{2-\mathrm{D}}$ becomes initially larger than $\rho_{1-\mathrm{D}}$; for greater distances from the star, however, it is smaller than $\rho_{1-\mathrm{D}}$. This phenomenon is caused by the radial dependence of $\mathrm{d}\mu/\mathrm{d}\mu_0$, $\dot M(\Theta_0)$ and $v_r(\Theta_0)$. As already pointed out, for small values of x only $\dot M(\Theta_0)$ and $\dot M_{1-\mathrm{D}}$ are different and determine exclusively the ratio $\rho(r,\Theta)/\rho_{1-\mathrm{D}}(r)$. For larger x and fixed Θ, the material originates from an initial co-latitude $\Theta_0 < \Theta$, since the particles were deflected towards the equatorial plane. According to Eq. (16), this is equivalent to a decrease in $\dot M(\Theta_0)$. Additionally, the ratio $v_r(r,\Theta)/v_{r,1-\mathrm{D}}(r)$ decreases for all Θ, (except at the pole, cf. Fig. 2), and $\mathrm{d}\mu/\mathrm{d}\mu_0$ is > 1 at the poles and < 1 near the equatorial plane (Fig. 4). It is now the combination of these three quantities that depend on x in different ways, which causes the ratio $\rho_{2-\mathrm{D}}/\rho_{1-\mathrm{D}}$ to become non-monotonic at intermediate co-latitudes.

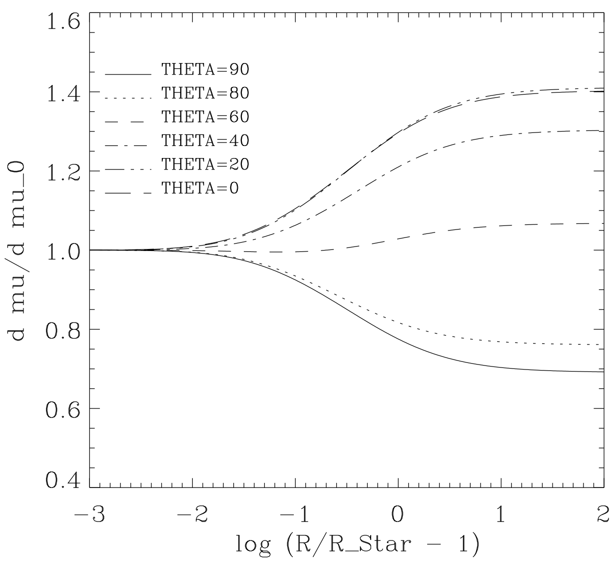

Fig. 4. As Fig. 2, but now for $\mathrm{d}\mu/\mathrm{d}\mu_0$ and $v_{\rm rot}$ = 300 km s^{-1}.

The effects of rotation on the hydrodynamical structure of typical O-star winds can be summarized as follows: Very close to the star and with the exception of the poles, where the radial expansion is always dominant, v_Φ significantly exceeds v_r and v_Θ. In contrast, v_Θ has sizable values only for a small radial interval at intermediate latitudes, though for extremely rapid rotators ($v_{\rm rot} \geq 300$ km s^{-1}) it may be the same order of magnitude as v_r. The deflection of the wind material towards the equatorial plane induced by this velocity component causes a density contrast between polar and equatorial regions, which increases both with distance from the star and rotational rate. This modified density structure will lead to significant consequences for the line formation process (§5.3), whereas the influence of v_Θ via the purely velocity-field dependent terms is restricted to the line core.

3.6. Gravity darkening

In the last section of this chapter, we will investigate the effects of gravity darkening, which may be expected to modify the contribution of the photospheric radiation field, both by its influence on the continuum and the photospheric line profile itself. As pointed out above, in our final models we will neglect the distortion of the stellar surface and any effects on the hydrodynamical structure by keeping the gravity and related quantities constant with respect to latitude. However, we will develop an approximate method which will allow us at least to account for *integral* effects caused by the lateral variation of the surface gravity.

Most aspects of our procedure are identical to those outlined by Cranmer & Owocki (1995, CO hereafter), and hence we will give only a brief summary.

3.6.1. Basic formulae

Due to the stellar rotation, the surface becomes distorted, and the stellar radius depends on co-latitude Θ (see CO, Eq. 26)

$$R_*(\Omega,\Theta) = \frac{3R_{\rm p}}{\Omega\sin\Theta}\cos\left(\frac{\pi + \arccos(\Omega\sin\Theta)}{3}\right). \qquad (19)$$

Here, $R_{\rm p}$ is the polar radius and assumed to be independent of the rotational velocity, i.e. used as input parameter. Ω is the normalized stellar angular velocity and defined by

$$\Omega \equiv \frac{\omega}{\omega_{\rm crit}} = \frac{1}{\omega_{\rm crit}}\frac{v_{\rm rot}}{R_{\rm eq}}, \qquad (20)$$

with angular velocity $\omega = v_{\rm rot}/R_{\rm eq}$ and the critical ("breakup") angular velocity $\omega_{\rm crit} = (8GM_{\rm eff}/(27R_{\rm p}^3))^{1/2}$, where we have accounted for the gravity reduction by Thomson scattering in replacing the stellar mass M_* by $M_{\rm eff} = (1-\Gamma)M_*$. $R_{\rm eq}$ is the radius at the equator ($\Theta = \pi/2$) and given by (CO, Eq. 27)

$$R_{\rm eq} = R_{\rm p}/(1 - v_{\rm rot}^2 R_{\rm p}/(2GM_{\rm eff})). \qquad (21)$$

The reader may note that the above definition of $\omega_{\rm crit}$ differs from the breakup velocity $\omega_{\rm crit,spherical} \equiv v_{\rm crit}/R_{\rm p}$ introduced in §3.4.1 owing to the neglect of the rotational distortion of the stellar surface.

We are primarily interested in the normal component of the gravity itself (and not the effective gravity corrected for Thomson scattering), since the appropriate photospheric fluxes/profiles are tabulated in terms of $T_{\rm eff}$ and $\log g$. This normal component of the gravity on the stellar surface is given by (see Collins 1965, Eqs. 4/5)

$$g_\perp(\Omega,\Theta) = \frac{GM_*}{R_{\rm p}^2}\frac{8}{27}\left[\left(\frac{27}{8}\frac{1}{\xi^2} - \xi\,\Omega^2\sin^2\Theta\right)^2 + \Omega^4\xi^2\sin^2\Theta\cos^2\Theta\right]^{1/2}, \qquad (22)$$

with normalized stellar radius $\xi \equiv R_*(\Theta)/R_{\rm p}$. The reader may note that this expression is implicitly dependent on $(1-\Gamma)$ via Ω and ξ. (Parenthetically and to avoid any confusion, we point out that in order to obtain the normal component of the *effective* gravity, one has to replace simply M_* by $M_{\rm eff}$ in Eq. 22.)

The above dependence of $g_\perp$ on Θ leads to a variation of the radiative flux $F(\Theta)$ emerging from the photosphere , which is proportional to $g_\perp$ via the von Zeipel theorem. If we consider, that

$$F(\Theta) = \sigma_{\rm B} T_{\rm eff}^4(\Theta), \qquad (23)$$

with $\sigma_{\rm B}$ the Stefan-Boltzmann constant and the local effective temperature $T_{\rm eff}(\Theta)$, we obtain

$$C(\omega)\, g_\perp(\omega,\Theta) = T_{\rm eff}^4(\Theta). \qquad (24)$$

$C(\omega)$ is the von Zeipel constant given by (Collins 1963, Eq. 13)

$$C(\omega) = \frac{L_*}{\sigma_{\rm B}}\Sigma^{-1}, \qquad (25)$$

where the surface-integrated value of $g_\perp$, Σ is:

$$\Sigma = \oint_A g_\perp(\omega,\Theta){\rm d}A = 2\pi\int_0^\pi g_\perp\left(\frac{R_*^2(\Theta)\sin\Theta{\rm d}\Theta}{-g_r/g_\perp}\right), \qquad (26)$$

and where g_r is the radial component of the gravity (CO, Eq. 28)

$$g_r = \frac{GM_*}{R_{\rm p}^2}\left(-\frac{1}{\xi^2} + \frac{8}{27}\,\xi\,\Omega^2\sin^2\Theta\right).$$

From Eqs. (25/26) it is clear that $T_{\rm eff}(\Theta)$ can be determined from the normal component of either the gravity or the effective gravity, as long as the $(1-\Gamma)$ dependence of Ω and ξ is correctly accounted for in *both* quantities.

Taking into account now the symmetry about the rotational axis, Eqs. (22), (24) and (26) provide the desired values for $g_\perp(\Theta)$ and $T_{\rm eff}(\Theta)$ at every location on the stellar surface.

This knowledge allows us now to pave the stellar surface with photospheric absorption profiles and continuum fluxes taken from grids that incorporate the dependence on $\log g_\perp(\Theta)$ and $T_{\rm eff}(\Theta)$. Thus, we can investigate the actual influence of gravity darkening on the observed profiles (see §5.1).

In order to compare line profiles calculated by neglecting gravity darkening with profiles including this effect, the former ones have to be calculated for a non-distorted "1-D comparison photosphere" with *averaged values* of radius $R_*^{\rm av}$, gravity $g_\perp^{\rm av}$ and effective temperature $T_{\rm eff}^{\rm av}$, since it is also this set of parameters which is underlying the photospheric spectroscopy of rotating stars by means of 1-D models. These averaged parameters can easily be determined, if we assume that rotating and non-rotating star have the same luminosity.

$$\begin{aligned} L_* &= \oint_A \sigma_{\rm B} T_{\rm eff}^4(\Theta)\,{\rm d}A \\ &= 4\pi \int_0^{\pi/2} \sin\Theta\, R_*^2(\Theta)\, \sigma_{\rm B} T_{\rm eff}^4(\Theta)\,{\rm d}\Theta \\ &=: 4\pi\,(R_*^{\rm av})^2 \int_0^{\pi/2} \sin\Theta\, \sigma_{\rm B} T_{\rm eff}^4(\Theta)\,{\rm d}\Theta. \end{aligned} \tag{27}$$

Thus we obtain for the averaged radius

$$R_*^{\rm av} = L_*^{1/2} \left(4\pi \int_0^{\pi/2} \sin\Theta\, \sigma_{\rm B} T_{\rm eff}^4(\Theta)\,{\rm d}\Theta \right)^{-1/2}, \tag{28}$$

and by means of

$$L_* = 4\pi (R_*^{\rm av})^2\, \sigma_{\rm B} (T_{\rm eff}^{\rm av})^4 \tag{29}$$

we can solve for $T_{\rm eff}^{\rm av}$. Finally, the averaged gravity required to choose the appropriate comparison profile is given by

$$g_\perp^{\rm av} = \frac{GM_*}{(R_*^{\rm av})^2}\,. \tag{30}$$

We will also use these averaged stellar parameters in our 2-D *wind* models in order to define both the electron temperature $T_{\rm e} \equiv 0.75\, T_{\rm eff}^{\rm av}$ and the core radius $R_* \equiv R_*^{\rm av}$.

3.6.2. Results for models including gravity darkening

By applying the method outlined above to our O-star model from § 3.5, we obtain the results listed in Table 1. We have compared the values for the surface-integrated gravity Σ (Eq. 26) with those obtained by using the fit formula provided by CO (their Eq. 32), where the deviations turned out to be less than $3 \cdot 10^{-3}$ in all cases.

By inspection of Tab. 1, we find that for low rotational velocities ($v_{\rm rot} \le 150$ km s^{-1}) the stellar distortion at the equator is less than 5% . If $v_{\rm rot}$ exceeds $\sim$ 300 km s^{-1}, the surface deformation reaches more than 20 %. The reader may note, however, that our O-type *Supergiant* model is a rather extreme case with a value of $\Gamma = 0.5$ implying a break-up velocity of $v_{\rm crit}$ = 420 km s^{-1}. For O-type main sequence stars with the largest observed rotational rates, $v_{\rm crit}$ lies well above 500 km s^{-1}. Thus, the approximation of a spherical stellar surface should be dropped for rotational rates greater than 300 km s^{-1} or 400 km s^{-1} for supergiants and dwarfs, respectively.

Table 1. Stellar parameters and their averaged values as function of rotational speed. Equatorial radius $R_{\rm eq}$ and averaged radius $R_*^{\rm av}$ in units of $R_{\rm p}$, effective temperatures at the pole $T_{\rm eff,p}$, at the equator $T_{\rm eff,eq}$ and averaged effective temperatures $T_{\rm eff}^{\rm av}$ in K, $v_{\rm rot}$ in km s^{-1}. $g_{\perp,\rm eq}$ denotes the equatorial normal gravity.
Stellar parameters as in §3.5: Stellar luminosity $L_* = 10^6 L_\odot$, polar gravity $\log g_{\perp,\rm p}$ = 3.60, polar radius $R_{\rm p} = 19 R_\odot$, stellar mass $M_* = 52.5\, M_\odot$, Γ = 0.5, $v_{\rm crit}$ = 420 km s^{-1}.

$v_{\rm rot}$	$\log g_{\perp,\rm eq}$	$R_{\rm eq}$	$T_{\rm eff,eq}$	$T_{\rm eff,p}$	$R_*^{\rm av}$	$\log g_\perp^{\rm av}$	$T_{\rm eff}^{\rm av}$
0	3.60	1.00	42000	42000	1.00	3.60	42000
50	3.59	1.00	41870	42070	1.00	3.60	41940
100	3.57	1.02	41470	42270	1.01	3.59	41740
150	3.52	1.04	40760	42610	1.02	3.58	41420
200	3.46	1.08	39690	43110	1.05	3.56	40990
250	3.36	1.13	38120	43800	1.08	3.54	40480
300	3.22	1.20	35790	44670	1.11	3.51	39920
350	2.98	1.30	32060	45720	1.13	3.49	39430

For $v_{\rm rot} \lesssim 250\,{\rm km\,s^{-1}}$, the difference in $\log g_\perp$ and $T_{\rm eff}$ between pole and equator is quite moderate, namely $\lesssim 0.24$ dex in $\log g_\perp$ and $|T_{\rm eff,eq} - T_{\rm eff,p}|/T_{\rm eff,p} \le 0.13$, respectively. In particular, the averaged values of stellar radius $R_*^{\rm av}$ (larger than $R_{\rm p}$) and gravity $g_\perp^{\rm av}$ (lower than $g_{\perp,\rm pole}$) differ only weakly from their nominal values at zero rotational rate. Since all our models require the same luminosity, and the "effective" surface of the star is enlarged, the averaged effective temperature $T_{\rm eff}^{\rm av}$ decreases with increasing $v_{\rm rot}$.

4. Line formation

In this section we will outline our method of calculating line profiles on the basis of the 2-D models developed in §3 and investigate some basic effects introduced by accounting for the differential rotation in the line formation process.

4.1. Geometry

For our calculations, we used the geometry presented in Fig. 5. (For a detailed derivation of the expressions given below we refer the reader to Mazzali (1990), where however our coordinate system is slightly different from the one he used.) The observer's cartesian coordinate system is denoted by (z, p, q) and the inclined stellar system by (z_*, p_*, q_*). i denotes the inclination angle. The observer is located at $z = \infty$ and only receives radiation emitted into direction $\boldsymbol{n}_z$.

4.2. Projected velocities

As discussed in § 3.3, in the following we will neglect the polar velocity component, i.e., we set $v_\Theta \equiv 0$ and consider only the

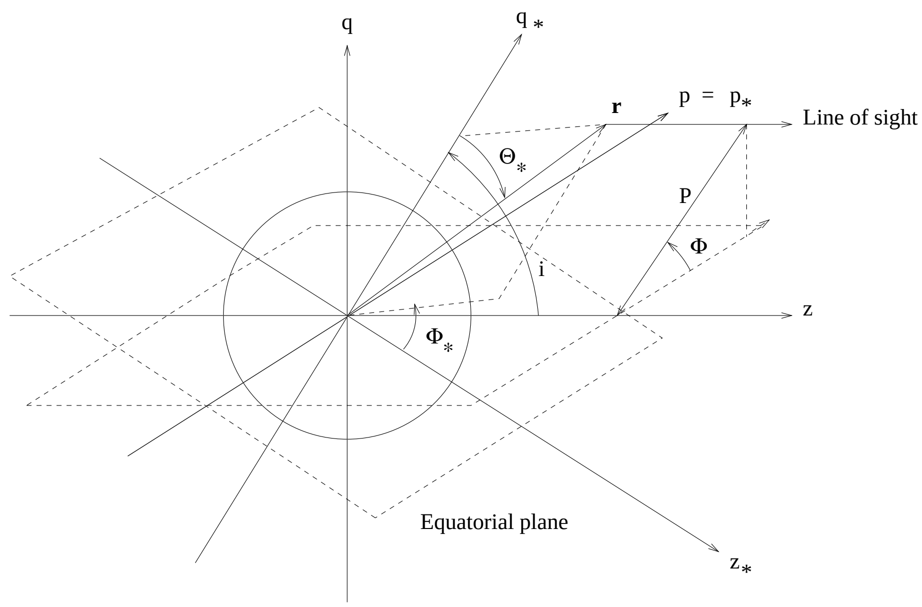

Fig. 5. Geometry used for calculating the formal integral. The stellar system (z_*, p_*, q_*) is inclined relative to the observer's system (z, p, q) by an inclination angle i. Note that $p_* = p$. The star rotates counter-clockwise about the q_*-axis, and the observer is located at $z = \infty$. Θ_* is the polar and Φ_* the azimuthal angle. The polar coordinates (P, Φ) are defined in the (p, q)-plane, with $p = P\cos\Phi$ and $q = P\sin\Phi$.

radial and azimuthal velocity components. With the unit normal vector in direction z, which is defined in stellar coordinates by

$$\boldsymbol{n}_z = (z_*(\boldsymbol{n}_z), p_*(\boldsymbol{n}_z), q_*(\boldsymbol{n}_z)) = (\sin i, 0, \cos i), \tag{31}$$

and the unit vectors $\boldsymbol{e}_{r_*}, \boldsymbol{e}_{\Phi_*}$

$$\boldsymbol{e}_{r_*}(\boldsymbol{r}) = \begin{pmatrix} \sin\Theta_*\ \cos\Phi_* \\ \sin\Theta_*\ \sin\Phi_* \\ \cos\Theta_* \end{pmatrix}, \ \boldsymbol{e}_{\Phi_*}(\boldsymbol{r}) = \begin{pmatrix} -\ \sin\Phi_* \\ \cos\Phi_* \\ 0 \end{pmatrix}, \tag{32}$$

the line of sight velocity in stellar coordinates is given by

$$\begin{aligned} \boldsymbol{n}_z\boldsymbol{v} \equiv v_{\rm obs} &= v_r\ (\sin i \sin\Theta_* \cos\Phi_* + \cos i \cos\Theta_*) \\ &\quad -v_\Phi\ \sin i \sin\Phi_*, \end{aligned} \tag{33}$$

with Θ_* the polar and Φ_* the azimuthal angle defined as usual. The geometric transformations between the stellar spherical polar and cartesian coordinates are given by

$$\begin{aligned} \sin\Theta_* &= \frac{\left(p_*^2 + z_*^2\right)^{1/2}}{r} & \cos\Theta_* &= \frac{q_*}{r} \\ \sin\Phi_* &= \frac{p_*}{\left(p_*^2 + z_*^2\right)^{1/2}} & \cos\Phi_* &= \frac{z_*}{\left(p_*^2 + z_*^2\right)^{1/2}}, \end{aligned} \tag{34}$$

where here and in the following we have omitted the subscript for the stellar coordinate r since this is only defined in the stellar frame.

Due to the stellar rotation, the photosphere also moves in space, with velocity $\boldsymbol{v}_{\rm phot}$. Its line of sight component (now measured as function of the observer's coordinates (P, Φ)) results in

$$\boldsymbol{n}_z\boldsymbol{v}_{\rm phot} \equiv v_{\rm phot} = -\ v_{\rm rot} \sin i\ \frac{P\cos\Phi}{R_*}. \tag{35}$$

The directional derivative of the velocity field along the line of sight (required for evaluating the Sobolev optical depth (Eq. 1)) is computed following the procedure by Mazzali (1990),

$$\frac{{\rm d}\,(\boldsymbol{n}_z\boldsymbol{v})}{{\rm d}\,\boldsymbol{n}_z} = \frac{v_r}{r}\left[1 + \left(\frac{z}{r}\right)^2\sigma + \frac{2\,v_\Phi \sin i\,p\,z}{v_r\ r\left(p_*^2 + z_*^2\right)^{1/2}}\right] \equiv \frac{v_r}{r}Q_0. \tag{36}$$

Here, the curvature parameter σ

$$\sigma = \left(\frac{\partial v_r}{\partial r} \Big/ \frac{v_r}{r}\right) - 1 = \frac{\partial \ln v_r}{\partial \ln r} - 1 \tag{37}$$

(introduced by Castor (1970)) measures the deviation of the purely radial from a homologous expansion, and the third term in Q_0 accounts for the additional influence of differential rotation on the velocity derivative. Note, that this term vanishes for $v_{\rm rot} \equiv 0$.

4.3. Influence of differential rotation on the optical depth

We will now discuss the extent to which differential rotation affects the crucial quantity in the line formation process, namely

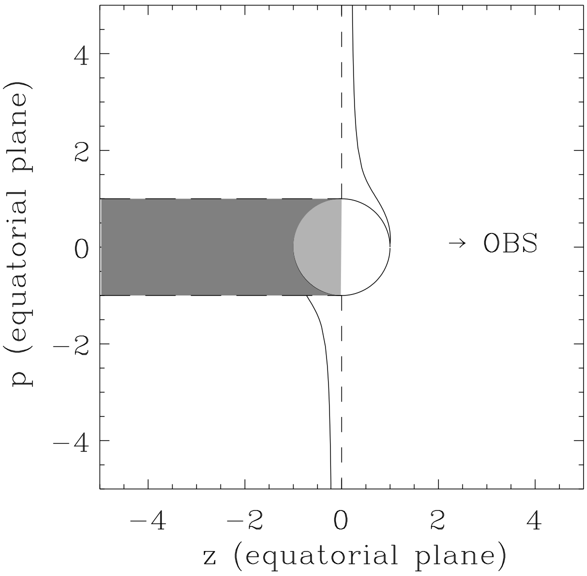

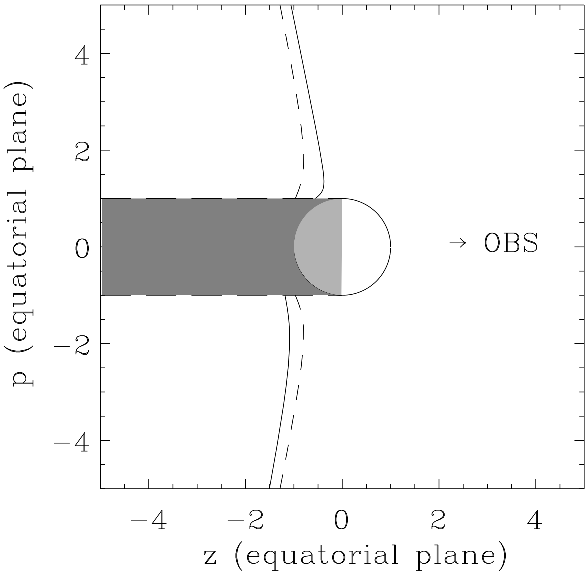

Fig. 6. Resonance zones (as "seen" by an observer, i.e. as functon of p) in a 2-D O-star wind in the equatorial plane for $X = 0$ (left) and $X = -0.2$ (right). Dashed: $v_{\rm rot} \equiv 0$, fully drawn: $v_{\rm rot} = 400\,\rm km\,s^{-1}$. Wind parameters: $v_{\rm min} = 20\,\rm km\,s^{-1}$, $v_\infty = 2250\,\rm km\,s^{-1}$ and $\beta = 1$. The hatched region behind the stellar core is occulted from the observer. In contrast to our usual notation, p and z are scaled in units of R_*.

the optical depth. To do so, we adopt a 1-D density stratification (Eq. 2) and a velocity field given by Eqs. (6) and (7). Due to the additional azimuthal velocity component, the location of the resonance zones and the local velocity gradient $\mathrm{d}\,(\boldsymbol{n}\boldsymbol{v})/\mathrm{d}\,\boldsymbol{n}$ in the wind are different from those for a purely radially expanding wind. According to Eq. (1), this modifies the Sobolev optical depth τ.

In order to find the location of the corresponding resonance zones as function of frequency, we have to solve for the *resonance condition*

$$X = \frac{\boldsymbol{n}_z\,\boldsymbol{v}}{v_\infty} = \frac{v_{\rm obs}}{v_\infty}, \tag{38}$$

where X measures the frequency displacement with respect to rest wavelength ν_0 in units of the maximum Doppler shift,

$$X = \frac{c}{v_\infty}\left(\frac{\nu}{\nu_0} - 1\right) \tag{39}$$

The projected velocity $v_{\rm obs}$ is obtained by inserting the expressions for v_r and v_Φ into Eq. (33)

$$v_{\rm obs} = v_r\,\frac{z}{r} - v_{\rm rot}\,\frac{p}{r}\frac{R_*}{r}\sin i\,, \tag{40}$$

and, after solving for the resonance zone (z, r) as function of (X, r), the directional derivative at this location follows from Eq. (36):

$$\frac{\mathrm{d}\,(\boldsymbol{n}_z\,\boldsymbol{v})}{\mathrm{d}\,\boldsymbol{n}_z} = \frac{v_r(r)}{r}\left[1 + \left(\frac{z}{r}\right)^2\sigma + \frac{2\,v_{\rm rot}\sin i\,p\,z\,R_*}{v_r(r)\,r^3}\right]. \tag{41}$$

Since the largest effects occur at the equator (cf. Eq. 7), we restrict the following considerations to this plane. In Fig. 6, we have plotted the resonance zones in a wind of a typical O-star for two different frequencies ($X = 0$ and $X = -0.2$) for $v_{\rm rot} \equiv 0$ and $v_{\rm rot} = 400\ \rm km\,s^{-1}$, respectively. The star rotates *counter-clockwise*, so that the wind material obtains an additional azimuthal velocity component away from (for $p > 0$) and towards (for $p < 0$) the observer. This consequently leads to a *clockwise* twist of the resonance zones near the core, i.e., contrary to the rotational sense of the star. As shown in Fig. 6, the resonance zones for $X \approx 0$ are essentially shifted away from the star (one has to compare the situation at the same impact parameter p), whereas for larger (absolute) values of X (right panel) half of the resonating material ($p > 0$) is moved closer towards the star.

This behaviour has important consequences for the optical depth. Since (cf. Eq. 3) $A^{'}(r)$ is an only mildly varying function of r, we will concentrate on the density/velocity dependence of $\tau \sim (r^3 v_r^3\,|Q_0|)^{-1}$. For low values of β, i.e. for a steep radial velocity law close to the star, v_r strongly grows with r in this wind region. As calculations have confirmed, $|Q_0|$ changes on the same scale as v_r, but due to the strong dependence on v_r, $\tau \sim v_r^{-3}$, this turns out to be the crucial quantity. In other words, it is primarily the density dependence which controls the behaviour of τ, as is to be expected for recombination lines. Hence, for small frequency displacements from line centre the optical depth is decreased due to the twist of the resonance zones away from the star, whereas it is (on the *average* and due to the strong dependence on ρ^2) enhanced for larger values of $|X|$. This behaviour of the resonance zones (and its consequences for the optical depth) will be called the *resonance zone effect* hereafter (cf. §5.2).

The reader may also note that in the case of our O-star models (i.e., large v_∞) even for large rotational rates *no multiple* resonance zones occur along a line of sight (Fig. 6, fully drawn curves).

4.4. Calculation of the line profile

The emergent flux $F_\nu^{\rm obs}$, measured by an observer at distance D from the star, is found by integrating the intensity $I_\nu^{\rm emg}$ over a plane perpendicular to the line of sight. $I_\nu^{\rm emg}$ is here the intensity emerging at the outer boundary of the wind $r_{\rm max}$ and directed towards the observer. Thus, we have

$$F_\nu^{\rm obs} = \frac{1}{D^2}\int_0^{2\pi}\int_0^{R_*} I_\nu^{\rm emg}(\Phi, P, \boldsymbol{n}_z) P \mathrm{d}P\, \mathrm{d}\Phi + \frac{1}{D^2}\int_0^{2\pi}\int_{R_*}^{r_{\rm max}} I_\nu^{\rm emg}(\Phi, P, \boldsymbol{n}_z) P \mathrm{d}P\, \mathrm{d}\Phi \tag{42}$$

The first term attributes the *core region*, and the second one the emission lobes (*non-core region*). By means of the Sobolev approximation, we obtain in the most general case (i.e., allowing for multiple resonances, but see above)

$$\begin{aligned} I_\nu^{\rm emg}(\Phi, P, \boldsymbol{n}_z) = \\ I_{\bar\nu}^{\rm c} \exp\left(-\sum_{i=1}^{N} \tau(\boldsymbol{r}_i', \boldsymbol{n}_z)\right) H(R_* - P) + \\ + \sum_{i=1}^{N} S(\boldsymbol{r}_i') \left[1 - \exp(-\tau(\boldsymbol{r}_i', \boldsymbol{n}_z))\right] \\ \times \exp\left(-\sum_{j=1}^{i-1} \tau(\boldsymbol{r}_j', \boldsymbol{n}_z)\right) \end{aligned} \tag{43}$$

(e.g., Rybicki and Hummer 1978). The Heaviside step-function H accounts for the fact that the observer can receive (processed) photospheric radiation (including line radiation) emitted by the star with intensity $I_{\bar\nu}^{\rm c}$ and frequency $\bar\nu$ only within the core region. $\bar\nu$ is (re-)corrected for the Doppler shift the particle experiences in the wind *and* for the rotation of the photosphere in the reference frame of the observer. It is given by

$$\bar\nu = \nu_0 \left(1 + \frac{v_{\rm obs} - v_{\rm phot}}{c}\right), \tag{44}$$

where $v_{\rm obs}$ and $v_{\rm phot}$ are defined as in Eq. (33/35). $\boldsymbol{r}_{i(j)}'$ denotes the resonance points in the wind with respect to frequency ν. $\boldsymbol{r}_j'$ are the points that are located between $\boldsymbol{r}_i'$ and the observer along the line of sight.

In order to calculate the normalized line profile $R_\nu = F_\nu^{\rm obs}/F_\nu^{\rm cont}$ we also need the continuum flux, which is given by

$$F_\nu^{\rm cont} = \frac{1}{D^2}\int_0^{2\pi}\int_0^{R_*} I_\nu^{\rm cont} P \mathrm{d}P\, \mathrm{d}\Phi\,. \tag{45}$$

In the following, we will usually assume that the photospheric continuum is constant over the line profile, $I_\nu^{\rm cont} \equiv B_{\nu_0}(T_{\rm rad})$ with $T_{\rm rad} = 0.77\, T_{\rm eff}$ at H$_\alpha$ (cf. Pu95).

However, in those cases where we explicitly account for gravity darkening, the calculation of both the photospheric profile and continuum requires some additional remarks. As pointed out in §3.6, we will neglect any deviation from sphericity when performing the formal integral, since the surface distortion was shown to be minimal in the O-star case (§3.6.2). Thus, in our 2-D transfer code we will adopt a spherical star with $R_*(\Theta_*) = R_*^{\rm av}, \forall\Theta_*$; however we use the local gravity $g_\perp(\Theta_*)$ (Eq. 22) and the local effective temperature $T_{\rm eff}(\Theta_*)$ (Eq. 24) at different locations on its surface.

With this simplification we can easily determine the continuum flux $F_\nu^{\rm cont}$ received by the observer. By using the geometry introduced in §4.1 and by neglecting limb darkening, $F_\nu^{\rm cont}$ comprises the average of all local continuum fluxes $F_\nu^{\rm cont}(\Theta_*)$ as function of $g_\perp(\Theta_*)$ and $T_{\rm eff}(\Theta_*)$, which are taken from a grid of plane-parallel NLTE model atmospheres (Herrero, priv. comm.)

$$F_\nu^{\rm cont} = \frac{1}{\pi R_*^2}\int_0^{2\pi}\int_0^{R_*} F_\nu^{\rm cont}(\Theta_*(P,\Phi))\, P \mathrm{d}P\, \mathrm{d}\Phi, \tag{46}$$

with

$$\Theta_*(P,\Phi) = \arccos(q_*(R_* = R_*^{\rm av}, P, \Phi, \sin i)). \tag{47}$$

q_* can be easily calculated:

$$\begin{aligned} q_* &= z \cos i + q \sin i \\ &= (R_*^{\rm av2} - P^2)^{\frac{1}{2}} \cos i + P \sin\Phi \sin i \end{aligned} \tag{48}$$

Finally, the normalized photospheric line profile $R_\nu^{\rm phot}$ is given by

$$R_\nu^{\rm phot}(P,\Phi) = \frac{F_\nu^{\rm phot}(\Theta_*(P,\Phi))}{F_\nu^{\rm cont}}, \tag{49}$$

where $F_\nu^{\rm phot}(\Theta_*)$ is the actual line flux emerging from the photosphere at co-latitude Θ_*. It is evident that $R_\nu^{\rm phot}(P,\Phi)$ is equivalent to $\pi R_*^2 \left(I_\nu^{\rm c}(\Theta_*)/F_\nu^{\rm cont}\right)$.

5. The line profiles

Having described the different models and methods of calculation in considerable detail, we will now investigate the implications for the resulting H_α-profiles. In particular, we will concentrate on the deviations from the conventional 1-D approach and the consequences for the determination of mass-loss rates and (as we will see below) *absolute* stellar rotational velocities $v_{\rm rot}$.

For our numerical calculations, we mapped the stellar (r, Θ)-plane with 400 radial grid points ranging from $r = R_*$ to $r = 100\,R_*$, which are logarithmically spaced. The polar grid consists of 91 equidistant points in Θ (with $\Theta \in [0, \pi/2]$ due to the present symmetry about the equatorial plane). This large number of grid points turned out to be essential in order to achieve the accuracy required for the conservation of mass-flux, but has no consequences on the computational time, which is constrained by the number of (P, Φ) points in the plane perpendicular to z. Here, we used 33 points for Φ (equidistant), 30 points for P in the core region (equidistant as well) and 50 points for P in the non-core region (logarithmically spaced).

The line profiles were calculated from Eqs. (42,43,46) for the formal integral, Eqs. (6), (7) and (2) for the 1-D velocity field and density stratification, and Eqs. (8) to (16) in the 2-D case, where the conservation of mass-flux is accounted for via Eq. (18).

5.1. Gravity darkening

At first, let us check the extent to which the resulting profiles depend on a detailed treatment of gravity darkening by comparing them with profiles calculated using a single photospheric input profile that is appropriate for the averaged photospheric parameters. For this purpose, we proceed as outlined in § 3.6, i.e., in both cases we adopt a 2-D wind model with radius $R_*^{\rm av}$ and effective temperature $T_{\rm eff}^{\rm av}$ (Eqs. 28/29), where the only difference is the choice of the photospheric input fluxes: for the "1-D comparison photosphere", we use an input profile appropriate to $g_\perp^{\rm av}, T_{\rm eff}^{\rm av}$, whereas in the "exact" approach we use profiles given by $g_\perp(\Theta), T_{\rm eff}(\Theta)$ and a continuum as defined by Eq. (46). Fig. 7 displays the results for a star with very low ($\dot M = 10^{-8} M_\odot {\rm yr}^{-1}$) and high ($\dot M = 6 \cdot 10^{-6} M_\odot {\rm yr}^{-1}$) mass-loss rate. Here and in the following profiles, we plot residual flux R_ν vs. frequency displacement X in units of the maximum Doppler shift with respect to v_∞, and have redefined the equivalent width to be positive for net emission.

In the first case, the wind emission is virtually zero, i.e., we observe the pure photospheric profile, whereas in the second one the wind emission clearly dominates. Leaving the discussion of the different line shapes as function of mass-loss rate and inclination angle to the next sections, the comparison between the profiles including and neglecting gravity darkening demonstrates that even for a rapidly rotating star the effects are small, with maximum differences in the line core (and the equivalent width) of only a few percent.

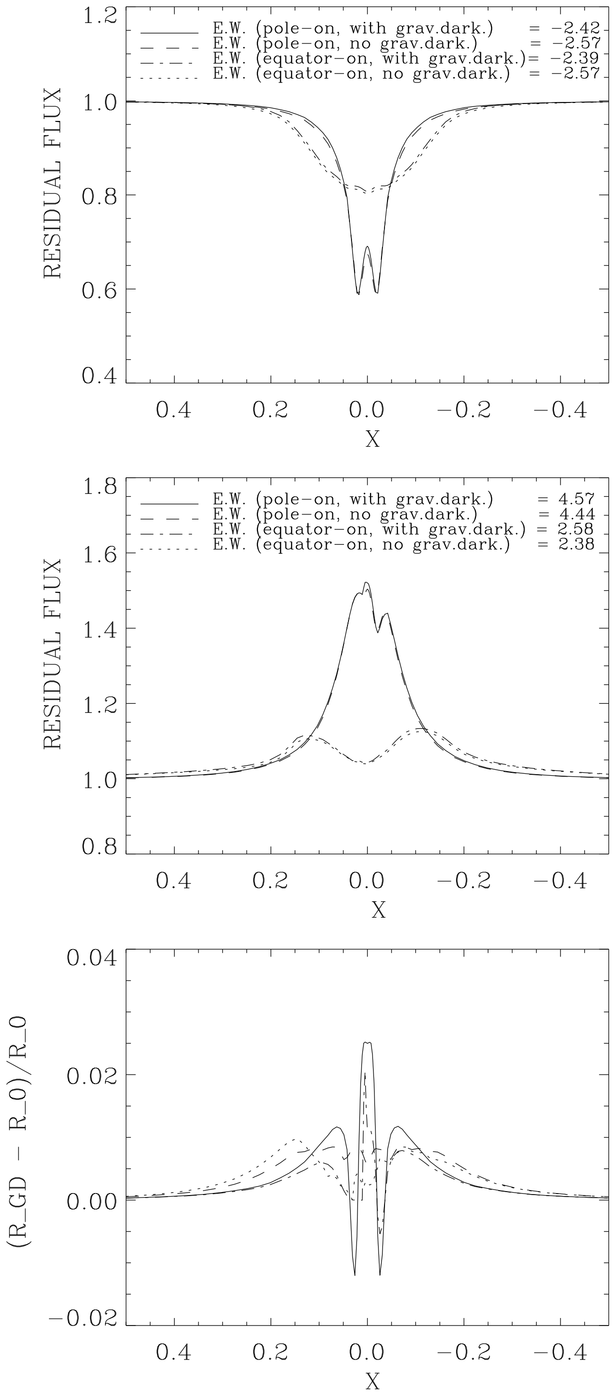

Fig. 7. H_α-line profiles for a 2-D density wind and stellar parameters as in Table 1 for $v_{\rm rot}$ = 300 km s^{-1}. Upper panel: $\dot M = 10^{-8} M_\odot {\rm yr}^{-1}$; fully drawn: $\sin i = 0$ (pole-on), with gravity darkening; dashed: $\sin i = 0$, no gravity darkening; dashed-dotted: $\sin i = 1$ (equator-on), with gravity darkening; dotted: $\sin i = 1$, no gravity darkening.
Middle panel: same as above, but for $\dot M = 6 \cdot 10^{-6} M_\odot {\rm yr}^{-1}$.
Lower panel: relative differences $(R_{\rm GD} - R_0)/R_0$ between H_α profiles including and neglecting gravity darkening. Fully drawn: $\dot M = 10^{-8} M_\odot {\rm yr}^{-1}$, $\sin i = 0$; dashed: $\dot M = 10^{-8} M_\odot {\rm yr}^{-1}$, $\sin i = 1$; dashed-dotted: $\dot M = 6 \cdot 10^{-6} M_\odot {\rm yr}^{-1}$, $\sin i = 0$; dotted: $\dot M = 6 \cdot 10^{-6} M_\odot {\rm yr}^{-1}$, $\sin i = 1$.

This small difference can be attributed to the fact that our "1-D comparison photosphere" exhibits a profile which is an average of the different absorption profiles which are actually emerging from the stellar surface. Near the hot poles of the star, these profiles are weaker, whereas in the cooler equatorial regions they are stronger than the averaged feature. So, for any arbitrary inclination angle i both effects will partially compensate each other, where the residual (Fig. 7, lower panel) is so small that the substantial effort to account for this effect is not justified, in view of the additional uncertainties. Hence, in the subsequent investigations we will neglect this effect and use in all cases a photospheric input profile that is independent of latitude.

As an additional comment, we point out that the above argumentation is only justified for those stars where the temperature and density contrast between the pole and the equator does *not* induce level populations that are too different in these regions. This is actually true for the O-star case considered here, but is no longer valid for rapidly rotating B-stars, where the lateral variation of the physical conditions has a much larger effect on the population structure (see e.g., Massa 1995, CO).

However, there is a second conclusion to be drawn from this investigation: Our results for the low mass-loss model shows that the usual procedure to derive photospheric parameters by fitting synthetic line profiles (convolved with the appropriate rotation profile) to the observations actually results in values which are in almost perfect agreement with the *averaged* values. Thus, the procedure outlined in § 3.6 can be reversed to obtain the parameters for the corresponding non-rotating star or the stellar mass, at least in cases where a guess of $\sin i$ is possible (e.g., Herrero et al. 1992; see also below).

According to this line of reasoning, it is also obvious that stars of different parameters will exhibit almost identical photospheric profiles, as long as their averaged (i.e., actually effective) photospheric parameters are the same. This behaviour motivates our further proceeding with the comparison of profiles resulting from different models and different rotational rates. In all cases, we will compare only models with the *same* averaged parameters, independent of their actual rotational rates. By doing so, we have the most direct possibility to investigate the pure effects of different wind physics on the resulting line profiles, because the "effective" photospheric conditions are assumed to be prespecified at their averaged value. Evidently, we will have to account for the "re-transformation" of the derived averaged parameters (by means of photospheric analyses) to the actual ones in the final application of the method.

5.2. The basic influence of differential rotation

The first point in our investigation of the influence of stellar rotation on the emergent profiles involves the purely kinematical effect on the resonance zones and their optical depths. This is done on the basis of the model presented in §3.3, namely a 2-D velocity field and appropriate directional derivative (Eqs. 36/37) with, however, a somewhat inconsistent 1-D density stratification.

For this purpose, Fig. 8 compares three profiles, namely the one obtained from 1-D radiative transfer and $v_{\rm rot}$ = 0 (dotted), the one obtained from the conventional treatment (1-D radiative transfer and subsequent convolution) (dashed, "convolved" with $v_{\rm rot} \sin i$ = 300 km s^{-1}) and the one resulting from a correct 2-D radiative transfer (fully drawn, $v_{\rm rot}$ = 300 km s^{-1}).

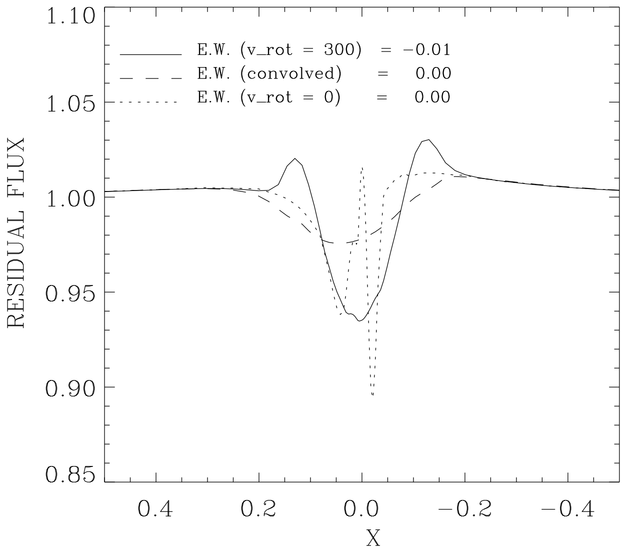

Fig. 8. H_α line profiles for a rotating wind model with a 1-D density stratification. Fully drawn: 2-D radiative transfer, 2-D velocity field with $v_{\rm rot}$ = 300 km s^{-1}; dotted: 1-D radiative transfer, $v_{\rm rot}$ = 0 km s^{-1}; dashed: 1-D radiative transfer and subsequent convolution with rotation profile of width $v_{\rm rot} \sin i$ = 300 km s^{-1}. $\dot{M}$ = $4.5 \cdot 10^{-6} M_\odot {\rm yr}^{-1}$, other parameters as in §3.5

Obviously, there are striking differences between the convolved and the exact 2-D profile. Compared to the non-rotating case, the convolved profile is broader and shallower due to the rotational broadening at *constant* rate, whereas the 2-D profile including differential rotation exhibits a much deeper absorption in the line core, while the wings show emission "humps". The reason for this behaviour is the resonance zone effect described in §4.3: at frequencies $|X| \gtrsim 0.1 \ldots 0.2$, the optical depth of the corresponding resonance zones is enlarged, while it is diminished near the line core $|X| \lesssim 0.1$. Since the source function remains (almost) constant, this is equivalent to an increase in emission in the line wings and a decrease in emission near the line centre, compared to the non-rotating case. E.g., the central emission present for $v_{\rm rot}$ = 0 is missing in the 2-D case, although the densities in our models are identical. Note, that the absorption widths of the non-rotating and the 2-D case coincide more closely with each other than do those of the 2-D case and the convolved one. This illuminates the fact that for this significant mass-loss rate the "effective" rotation rate lies closer to zero than to its photospheric value.

Since the profiles are influenced by (moderate) departures from LTE and an underlying photospheric absorption profile, these effects are clarified in Fig. 9, on the basis of a line in pure LTE, no photospheric profile and $T_e = T_{rad} \equiv 0.75\,T_{eff}$ (i.e., $I^c_\nu = B_\nu(T_{rad}) = B_\nu(T_e) = S(r'_i)$). In this case and according to Eq. (43), the contribution of the core region is identical to zero, since no multiple resonances are present and the emission/absorption processes completely cancel each other in front of the stellar core. Thus, we see the pure emission of the lobes, so that in this model the resonance zone effect alone is manifest: With increasing v_{rot}, the central emission decreases, whereas the wings increase. For extreme rotational rates ($v_{rot} \gtrsim 300\,\mathrm{km\,s^{-1}}$), two emission maxima appear blue- and redwards from the line centre. Note that *no* "disk" underlies this feature.

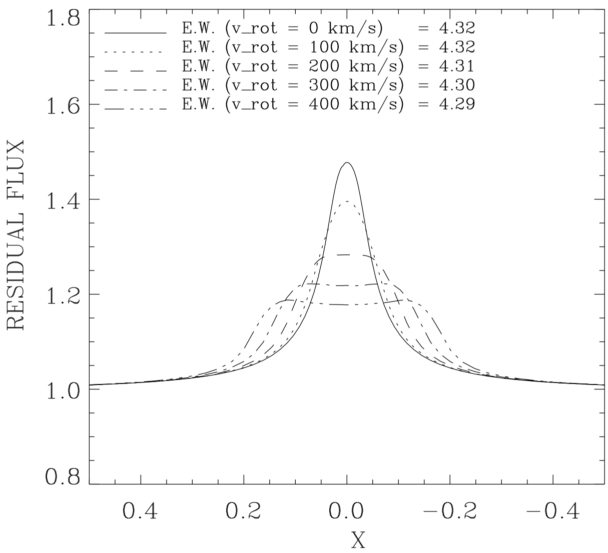

Fig. 9. H_α profiles for 1-D density, 2-D velocity field and 2-D radiative transfer: line in LTE (i.e., $b_2(r), b_3(r) \equiv 1$), $T_e = T_{rad} = 0.75\,T_{eff}$, $\sin i = 0$, no photospheric absorption. $\dot{M} = 6 \cdot 10^{-6} M_\odot \mathrm{yr}^{-1}$, other parameters as in §3.5.

The difference between the 1-D convolved and the 2-D profiles is most significant for a low absolute equivalent width $|W_\lambda| \approx 0$, when absorption and emission are roughly equal. In this case, the resonance zone effect has the largest impact on the profile *shape*; for strong emission profiles, the effect is weaker since the emission comes from a larger volume, where the average shift of resonance zones is smaller (Fig. 6), whereas profiles with a dominant absorption component by definition are affected only weakly by the wind physics.

The marked difference between convolved and 2-D profiles with $|W_\lambda| \approx 0$ (even neglecting the change in wind density) has severe consequences for line fits obtained with the conventional 1-D approach. If we want to reproduce the deeper and narrow central absorption (cf. also Fig. 17d for profiles including a consistent density structure) by means of the inappropriate 1-D approach, we would have to adopt a projected rotational velocity $v_{rot} \sin i$ *lower* than the actual value (cf. Pu95, who actually found this effect for a number of stars with large $v_{rot} \sin i$). But even then, we still would not have reproduced the emission peaks in both wings.

It has to be stressed that both the line of sight velocity v_{obs} (Eq. 40) and the corresponding directional derivative $\mathrm{d}(\boldsymbol{nv})/\mathrm{d}\,\boldsymbol{n}$ (Eq. 41) depend only on the projected rotational velocity $v_{rot} \sin i$ and not on the absolute value of v_{rot}. Consequently, it is not possible to derive $\sin i$ from the line profiles calculated so far, which account for a 1-D density only.

Finally, we point out an interesting property of the above profiles. Since the adopted spherically symmetric density structure is not affected by differential rotation, the *total* number of emitted photons is not modified compared with the non-rotating case. Thus, we expect the equivalent width to be conserved under the purely kinematical effects of rotation, as is actually found in Fig. 10. Hence, at least in cases with not too large absolute rotational velocities, where the density structure is only mildly modified, methods that determine mass-loss rates from *equivalent widths* (e.g., Leitherer 1988a, LL93, Pu95) are not affected by the resonance zone effect.

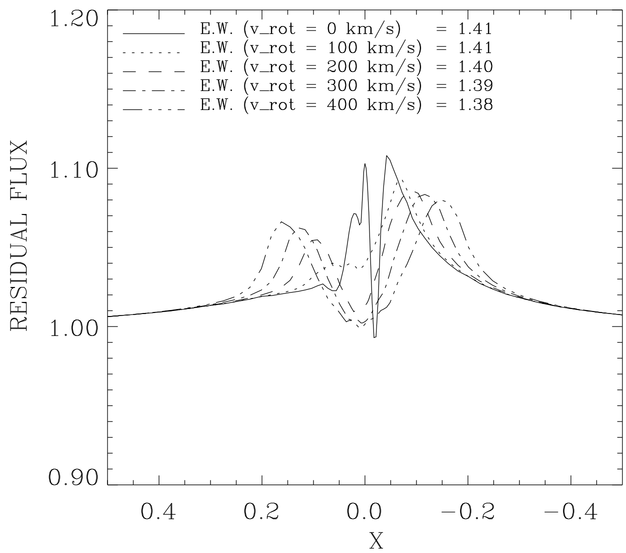

Fig. 10. H_α profiles calculated with 2-D radiative transfer for different v_{rot}, $\dot{M} = 6.0 \cdot 10^{-6} M_\odot \mathrm{yr}^{-1}$ and $\sin i = 1.0$. Other parameters as in §3.5. The equivalent width is conserved under differential rotation, if we assume a 1-D density wind.

5.3. 2-D density stratification

In the last step of our investigation, we present the results for our most consistent models, i.e., in addition to the differential rotation (again: $v_\Theta \equiv 0$) we account for the corresponding change in density by means of the BC model, as outlined in §3.4.

Since these models predict a density concentration in the wind from the pole towards the equatorial plane, the major part of the emission should originate in this region. For a given $v_{\rm rot} \sin i$ (from photospheric lines), then, the emergent profiles will explicitly depend on inclination angle i, since the density structure is a function of the absolute rotational velocity $v_{\rm rot}$. This provides us with a possibility to determine $\sin i$ from H_α line fits in the winds of hot stars, as will become obvious in the following sections.

5.3.1. Basic effects

First, we will investigate the influence of the 2-D density structure on H_α line profiles as a function of $v_{\rm rot}$ (while holding the inclination angle constant) and as a function of $\sin i$ (holding $v_{\rm rot}$ constant). The case of constant $v_{\rm rot} \sin i$, which is the most interesting with respect to the analysis of observed profiles, will be discussed later.

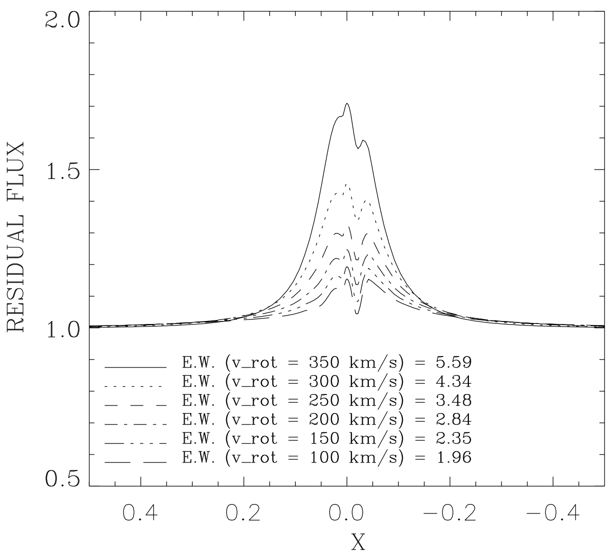

Fig. 11. H_α profiles for a wind model with a 2-D density stratification, observed pole on, as function of rotational velocity $v_{\rm rot}$. $\dot{M} = 6 \cdot 10^{-6} M_\odot {\rm yr}^{-1}$, other parameters as in §3.5.

Constant $\sin i$. To demonstrate the pure effects of the density contrast, in Fig. 11 we have plotted H_α profiles for different rotational velocities $v_{\rm rot}$ *observed pole on*, i.e., $\sin i = 0$. Thus, the azimuthal velocity component is irrelevant for the line formation (cf. Eq. 33), and we have to consider only the radial component, so that the resonance zone effect is suppressed. Note, that here and in the following the surface integrated mass-loss rate is assumed to be equal for all $v_{\rm rot}$ in order to facilitate the comparison between the different 2-D and 1-D models (cf. §3.5). Hence, it is only the angular distribution of the outflow which differs as function of $v_{\rm rot}$. Since we observe the wind pole on, we see the maximum emitting area of the equatorial "compression zone".

Obviously, the emission at most frequencies, and accordingly the equivalent width, grows with increasing $v_{\rm rot}$. This effect, which is due to the increasing concentration of wind material towards the equatorial plane, leads to a strongly nonlinear increase in emission via ρ^2. In the following we will call this effect the *ρ^2-effect*.

For larger values of $v_{\rm rot}$, the differences in the shape and strength of successive profiles become increasingly more pronounced because the ρ^2-effect becomes very strong as $v_{\rm rot}$ approaches $v_{\rm crit}$. For example, for our model with $v_{\rm rot} = 100\,{\rm km\,s^{-1}}$, the density constrast is $\rho^2_{\rm equator}/\rho^2_{\rm pole} \lesssim 1.6$ (Fig. 3 (left)), whereas with $v_{\rm rot} = 300\,{\rm km\,s^{-1}}$ it reaches a value $\rho^2_{\rm equator}/\rho^2_{\rm pole} \lesssim 16$ (Fig. 3 (right)).

For frequencies $|X| \gtrsim 0.15$, the emission becomes smaller than in the 1-D case and decreases with increasing $v_{\rm rot}$. This is due to the fact that the emitting high velocity material (from polar regions for $\sin i = 0$) becomes thinner at the expense of the equatorial wind, when the star rotates faster and faster. Compared to the increase of the peak, however, this effect is small, since already for a 1-D density wind the contribution of the wing emission is quite low.

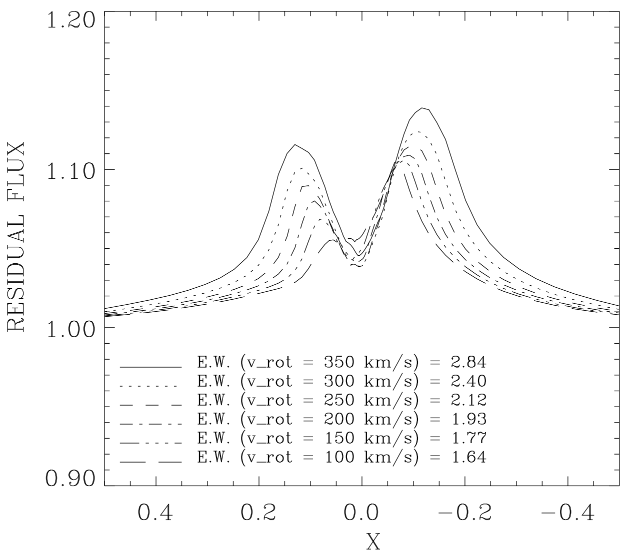

Fig. 12. As Fig. 11, but now observed equator on, i.e., $\sin i = 1$.

In Fig. 12, we see the same wind in H_α as before, however viewed *equator on*. The differences to Fig. 11 are striking. Firstly, the differences with increasing $v_{\rm rot}$ are much smaller, which is due to the fact that the contribution of the quasi-disk to the total emission is smallest in this configuration. Secondly, the familiar double-peaked shape points clearly to the resonance zone effect, which is most effective when $i \approx 90°$. In the next paragraph, we will pin down this behaviour more precisely.

Constant $v_{\rm rot}$. For this purpose, in Fig. 13 we display profiles for different $\sin i$ and $v_{\rm rot} = 250\,{\rm km\,s^{-1}}$. The equivalent width W_λ grows with decreasing $\sin i$, which is caused by the high

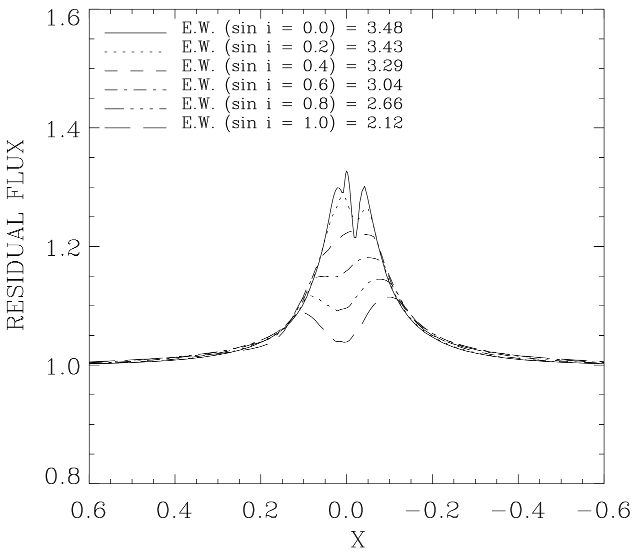

Fig. 13. As Fig. 11, but now for constant $v_{\rm rot}$ = 250 km s^{-1} and variable inclination $\sin i$.

efficiency of the ρ^2-effect for low inclinations. However, the line *wings* are almost identical.

This is caused by the combination of the ρ^2- and resonance zone effect, which is clarified in Fig. 14. If the wind is observed pole on, the wing emission is *exclusively* enlarged by the ρ^2-effect, which is not as important for higher inclinations, as follows from the comparison between the 1-D/2-D density models (Fig. 14, lower panel). In this case, however, the twist of the resonance zones becomes decisive and leads – in both models – to the enhanced wing emission, as discussed in in § 5.2.

This twist is even more pronounced at high stellar co-latitudes in our 2-D density model, since the radial velocity field depends on Θ_0 via of v_∞(Eqs. 10, 17). Thus, the radial velocity of the equatorial outflow is less than $v_{r,1-{\rm D}}$, whereas the twist is controlled by the ratio v_Φ/v_r.

Consequently, we find the profile wings in our 2-D density models to be almost independent of $\sin i$, where the lack of emission due to the reduced ρ^2-effect is compensated by the effects of differential rotation. Hence, for given $\dot M$ the profile wings are almost exclusively determined by $v_{\rm rot}$!

Finally, the apparent double peaked structure of the profiles for $\sin i \lesssim 0.2$ and $\sin i \gtrsim 0.8$ are – as in our 1-D density model – due to the resonance zone effect for large $\sin i$ and due to NLTE-effects at low velocities for small $\sin i$. This can be easily seen by disentangling the core and non-core contribution, which are plotted separately in Fig. 15. Obviously, with increasing $\sin i$ the total emission in the lobes is reduced (diminished ρ^2-effect) and the peak that is present for low $\sin i$ becomes essentially flat (resonance zone effect). The core contribution is mainly affected by photospheric absorption, which becomes rotationally broadened for higher $\sin i$.

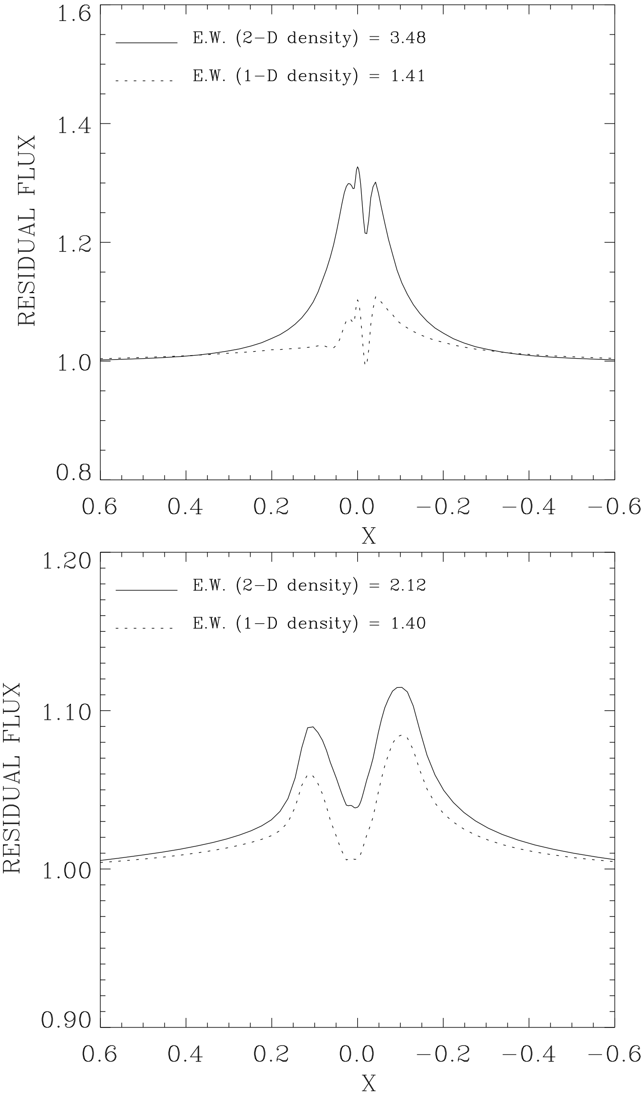

Fig. 14. Profiles for wind models with 2-D (fully drawn) and 1-D (dashed) density distribution. $v_{\rm rot}$ = 250 km s^{-1}, $\dot M$ = $6 \cdot 10^{-6} M_\odot {\rm yr}^{-1}$, other parameters as in §3.5. Upper panel: $\sin i$ = 0; lower panel: $\sin i$ = 1. The differences are more pronounced for $\sin i$ = 0.

5.3.2. Parameter study

One of the basic goals of this paper is to examine the extent to which the consistent inclusion of stellar rotation in O-star wind models modifies the mass-loss rate determined from H_α. For this purpose, we studied the dependence of the H_α profiles on the parameters $\dot M$ and $v_{\rm rot}$, and discuss the following two aspects: From the theoretical point of view, it is interesting to investigate the profile morphology for constant $v_{\rm rot}$ as a function of inclination angle. On the other hand, the actual application to the derivation of mass-loss rates necessitates an investigation with respect to constant $v_{\rm rot} \sin i$, as a function of the absolute rotation rate (and, of course, for compensating values of $\sin i$).

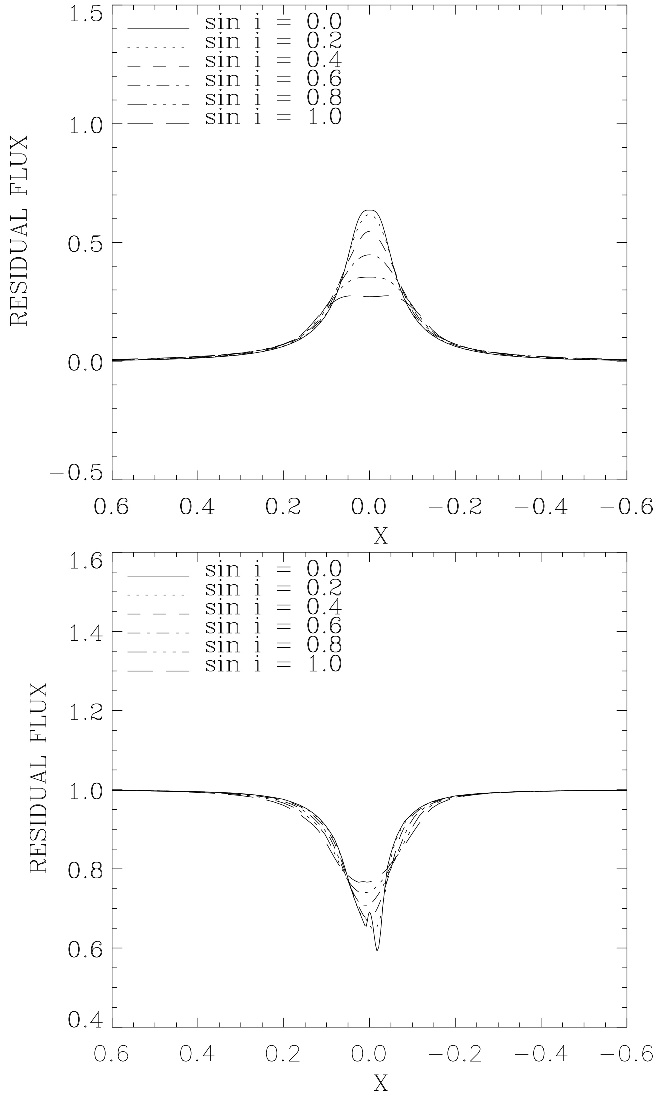

Fig. 15. As Fig. 13, but now for the contribution of the non-core (upper panel) and core region (lower panel).

Constant $v_{\rm rot}$. Figure 16 shows synthetic H_α profiles for $v_{\rm rot}$ = 100 km s^{-1}, 300 km s^{-1} and $\dot{M} = 10^{-6}, 3 \cdot 10^{-6}, 6 \cdot 10^{-6}\, M_\odot {\rm yr}^{-1}$, calculated by means of our 2-D density model and with *averaged* photospheric parameters as in §3.5, i.e., for a typical O-Supergiant.

In the case of low $v_{\rm rot}$ = 100 km s^{-1}, we find a significant change in equivalent width – both as function of inclination angle and compared with the conventional 1-D model – only for the highest mass-loss rate displayed, $\dot{M} = 6 \cdot 10^{-6}\, M_\odot {\rm yr}^{-1}$, where the ρ^2-effect is most effective. Changes are mostly confined to line center, while the profile wings remain essentially unaffected for all $\dot{M}$ at this low rotational rate. Note that for the models with the lowest mass-loss rate, the profile *shapes* hardly deviate from those calculated by the conventional convolution method, even though the projected rotational velocity $v_{\rm rot} \sin i$ changes from zero to $v_{\rm rot}$.

This is also true for the model with low $\dot{M}$ and large $v_{\rm rot}$ = 300 km s^{-1}, because the wind is too thin to cause significant emission. The only effect on the profile shape originates from the rotational broadening of the photospheric component, again in agreement with the simple approach.

For larger $\dot{M}$ and $v_{\rm rot} \gtrsim$ 200 km s^{-1}, however, the wind density and the rotational rate become large enough that the ρ^2- and the resonance zone effect are decisive. As discussed in §5.3.1, their combination causes almost identical wings for $|X| \gtrsim 0.15$, whereas the line cores are very discrepant. For the pure emission profile ($\dot{M} = 6 \cdot 10^{-6}\, M_\odot {\rm yr}^{-1}$), finally, the large increase in equivalent width when viewed under smaller and smaller angles is primarily due to the increased emission efficiency of the condensed equatorial material in the observer's direction.

In any case, however, we find the following systematic behaviour of the equivalent width:

- the equivalent width grows for given $\dot{M}$ and $\sin i$ as a function of $v_{\rm rot}$.
- the equivalent width decreases for given $\dot{M}$ and $v_{\rm rot}$ as a function of $\sin i$.
- (Obviously, the equivalent width grows for given $v_{\rm rot}$ and $\sin i$ as a function of $\dot{M}$.)

Constant $v_{\rm rot} \sin i$. As it is the quantity $v_{\rm rot} \sin i$ which can be inferred from "purely" photospheric lines, we finally show synthetic profiles with constant $v_{\rm rot} \sin i$ at different rotational rates (and corresponding angles) in order to permit comparison with observations. (Recall, however, that in this first investigation we have neglected the He-blend.) In Fig. 17, we display H_α profiles for $v_{\rm rot} \sin i$ = 50 and 200 km s^{-1} for $\dot{M} = 10^{-6}, 3 \cdot 10^{-6}$ and $6 \cdot 10^{-6}\, M_\odot {\rm yr}^{-1}$.

In contrast to what might be expected, the largest discrepancies arise for low $v_{\rm rot} \sin i$ values, since these include the possibility that the star is a rapid rotator observed approximately pole on. This in turn leads to the maximum possible emission, as we have seen above (large $v_{\rm rot}$ *and* low $\sin i$!). If instead we observe the same star at large inclination, this implies a low rotational velocity, and thus the equivalent width has its minimum value (low $v_{\rm rot}$ observed equator on, which is compatible with the 1-D approach).

For larger values of observed $v_{\rm rot} \sin i$, the variations with $\sin i$ are not as dramatic, since in this case it is most probable that we observe the star equator on, or at least with not too small $\sin i$; a lower limit on i can be set by requiring that $v_{\rm rot} \le v_{\rm crit}$. Hence, although we have a wind with a strong density contrast due to the large $v_{\rm rot}$, we observe it equator on, where the enhanced equatorial emission is partly compensated by the diminished emission from the other regions.

As already mentioned in § 5.2, a number of profiles from winds with not too large $\dot{M}$ and significant $v_{\rm rot} \sin i$ exhibit emission humps blue- and redwards from the absorption component (e.g., Fig. 17d), mainly due to the resonance zone effect. This may be an important result since a number of rotating stars *actually* show these features. E.g., the H_α profile of ξ Per = HD 24912 which has a photospheric value of $v_{\rm rot} \sin i$ = 250 km s^{-1} and a (1-D) mass-loss rate

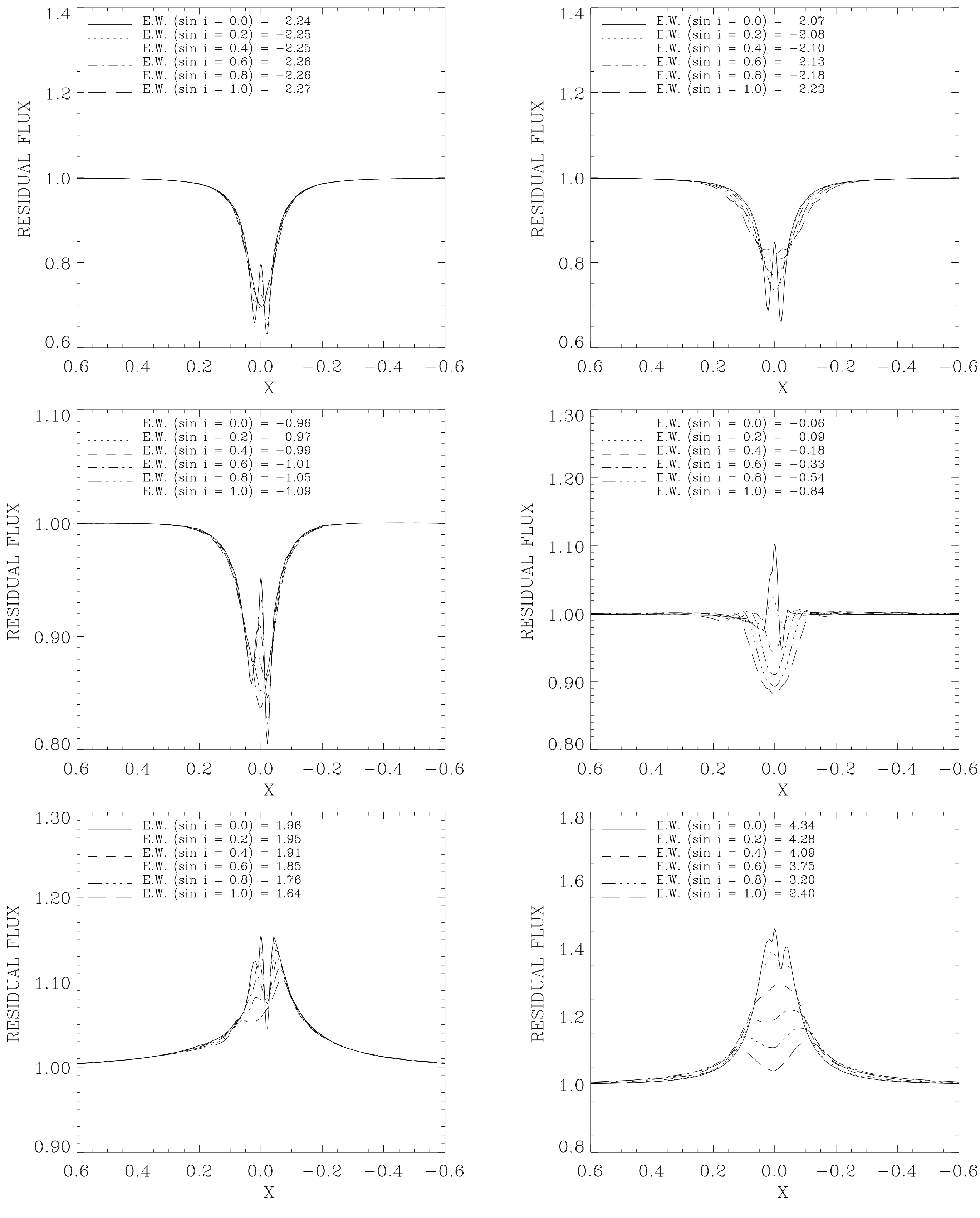

Fig. 16. H_α profiles for a typical O-Supergiant, for constant rotational rate and observed under varying inclination angles. Left panel: $v_{\rm rot}$ = 100 km s^{-1}; right panel: $v_{\rm rot}$ = 300 km s^{-1}. Upper panel: $\dot{M} = 10^{-6} M_\odot {\rm yr}^{-1}$, equivalent width for corresponding non-rotating star is −2.3Å; middle panel: $\dot{M} = 3 \cdot 10^{-6} M_\odot {\rm yr}^{-1}$, e.w.($v_{\rm rot}$ = 0) = −1.17Å; lower panel: $\dot{M} = 6 \cdot 10^{-6} M_\odot {\rm yr}^{-1}$, e.w.($v_{\rm rot}$ = 0) = 1.40Å. Other parameters as in §3.5.

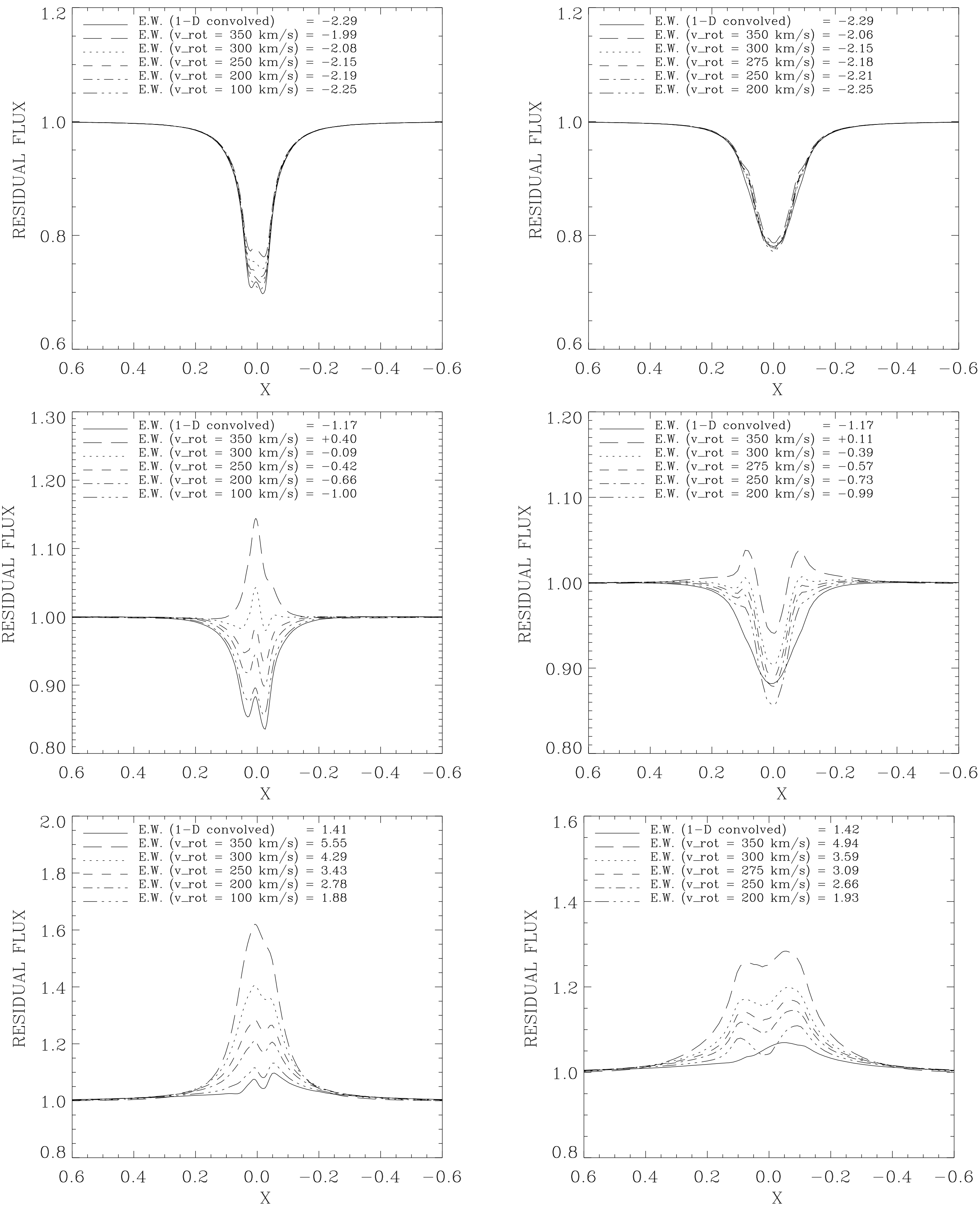

Fig. 17. H$_\alpha$ profiles for a typical O-Supergiant, for constant projected rotational velocity $v_{\rm rot}\sin i$, as a function of rotational rate $v_{\rm rot}$. Left panel: $v_{\rm rot}\sin i = 50\,{\rm km\,s^{-1}}$; right panel: $v_{\rm rot}\sin i = 200\,{\rm km\,s^{-1}}$. $\dot M = 10^{-6} M_\odot {\rm yr}^{-1}$ (upper panel), $3\cdot 10^{-6} M_\odot {\rm yr}^{-1}$ (middle panel) and $6\cdot 10^{-6} M_\odot {\rm yr}^{-1}$ (lower panel). Other parameters as in §3.5. Also indicated are the profiles that result from the conventional 1-D approach with subsequent convolution (fully drawn).

$\dot{M} \approx 3.2 \cdot 10^{-6} M_\odot \mathrm{yr}^{-1}$ (i.e., with similar parameters as the model illustrated in Fig. 17d), has a striking similarity with the profiles with intermediate $v_{\rm rot}$ in this figure (cf. Pu95). In particular, besides the observed emission humps, it exhibits an absorption width corresponding to $\approx 100\,\mathrm{km\,s^{-1}}$, much smaller than $v_{\rm rot} \sin i$, in accord with the displayed synthetic profiles. (In the course of the H_α analysis by Pu95, the latter discrepancy turned out to be typical for stars with large $v_{\rm rot} \sin i$.) Unfortunately, a detailed line fit has to be postponed to a follow-up paper since ξ Per has a rather large He abundance $Y = 0.22$.

Finally, we mention that the equivalent widths of the profiles that result from a corresponding 1-D treatment (fully drawn in Fig. 17) always have the *lowest* values. Thus, in any case, the ρ^2-effect leads to an enhanced emission when accounting for a consistent density structure.

5.3.3. Implications for the determination of $\dot{M}$

Although this first paper does not aim to check the influence of stellar rotation on the determination of $\dot{M}$ *by detailed line fits*, we will estimate the maximum difference which may arise by using either our consistent or conventional methods.

This will be done by using the scaling relation for the equivalent widths for 1-D models, as provided by Pu95. For the limit of optically thin emission, which is valid throughout the O-star domain, they found that $\dot{M}$ scales as follows (Pu95, Eq. 42):

$$\dot{M}(\mathrm{thin}) \sim W_\lambda^{'\,2/3} R_*^{3/2} v_\infty^{5/6}, \tag{50}$$

where W'_λ is the equivalent width, corrected for the photospheric absorption $|W_\lambda^{\rm phot}|$

$$W'_\lambda = W_\lambda + \left| W_\lambda^{\rm phot} \right| .$$

By neglecting the lateral dependence of the terminal velocity, we thus can estimate the error we introduce by performing a 1-D synthesis of a 2-D profile.

Let $\dot{M}$ denote the actual mass-loss rate and $W_{\lambda,2-\mathrm{D}}$ the corresponding equivalent width accounting for stellar rotation. We *do not* know the scaling relation between these two quantities, but we know that the equivalent width $W_{\lambda,1-\mathrm{D}}$ of the profile from a 1-D model with $\dot{M}$ (e.g., the fully drawn curves in Fig. 17) scales with $\dot{M} \sim W'_{\lambda,1-\mathrm{D}}(\dot{M})^{2/3}$. On the other hand the mass-loss rate $\dot{M}_{1-\mathrm{D\,fit}}$, which would follow from a 1-D analysis of the actual profile with equivalent width $W'_{\lambda,2-\mathrm{D}}$, is given by $\dot{M}_{1-\mathrm{D\,fit}} \sim W'_{\lambda,2-\mathrm{D}}(\dot{M})^{2/3}$, due to the incorrect neglect of the stellar rotation. Thus, the ratio of the mass-loss rate derived by the inappropriate 1-D fit and the actual one is simply given by

$$\frac{\dot{M}_{1-\mathrm{D\,fit}}}{\dot{M}} \approx \left(\frac{W'_{\lambda,2-\mathrm{D}}}{W'_{\lambda,1-\mathrm{D}}} \right)^{2/3}, \tag{51}$$

and since the ratio $(W'_{\lambda,2-\mathrm{D}}/W'_{\lambda,1-\mathrm{D}})$ is always larger than unity, the mass-loss rate from the 1-D fit will always *overestimate* the actual one. From our results of Fig. 17, we find as maximum errors the values listed in Tab. 2, which are valid for a typical O-Supergiant with an equivalent width of the photospheric profile (re-corrected for the missing He blend) $W_\lambda^{\rm phot} \approx -2.5$Å. From these results, it is obvious that the values we derive for the mass-loss rate by performing a 1-D analysis are at most 50 . . . 70% too large.

If we also consider that the average value of $< \sin i >= \pi/4$, then, for the case of an observed $v_{\rm rot} \sin i = 200\,\mathrm{km\,s^{-1}}$, the expectation value of the absolute rotational value is given by 256 km s^{-1}. From Fig. 17 and Eq. (51), we find that applying the 1-D method produces a *typical* error of 20 . . . 30%, whereas the typical error for $v_{\rm rot} \sin i \lesssim 100\,\mathrm{km\,s^{-1}}$ is almost negligible.

Table 2. Maximum errors in the determination of $\dot{M}$ performed by a 1-D analysis. Given are the ratios $\dot{M}_{1-\mathrm{D\,fit}}/\dot{M}$ as defined by Eq. (51), as a function of the actual mass loss rate $\dot{M}$. $v_{\rm rot} \sin i$ in km s^{-1}, $\dot{M}$ in $10^{-6} M_\odot \mathrm{yr}^{-1}$.

$v_{\rm rot} \sin i$	$\dot{M} = 1$	$\dot{M} = 3$	$\dot{M} = 6$
50	1.7	1.7	1.7
100	1.7	1.6	1.6
200	1.6	1.6	1.5
300	1.4	1.4	1.4

6. Summary, conclusions and future work

In the present paper, we have investigated the influence of stellar rotation on H_α line formation in O-star winds. For this purpose, we have disentangled the effects of both the modified velocity field and density structure. The wind model used is based on the kinematical approach provided by BC, adapted to the parameter space considered in this paper. We have discussed only cases with rotational rates well below those that would induce the onset of disk formation.

The large density contrast between the equator and pole that develops in the 2-D models for increasing values of $v_{\rm rot}$ is the essential ingredient for the effects summarized below. E.g., for rather low rotational rates ($\approx 100\,\mathrm{km\,s^{-1}}$), the *squared* contrast obtains values $\lesssim 1.6$, whereas for $v_{\rm rot} \approx 300\,\mathrm{km\,s^{-1}}$ it reaches values up to ten times larger. As a considerable simplification for our investigations, we found that the polar velocity component can be neglected compared with the azimuthal one *in the treatment of line formation*, because in all important cases the latter clearly dominates, at least if the purely kinematical model is applied.

Since it is well known that stellar rotation also influences the *photospheric* structure by distorting the otherwise spherical surface and inducing a lateral dependence of $R_*(\Theta), \log g(\Theta)$ and $T_{\rm eff}(\Theta)$ (the latter via the von Zeipel theorem), we have also investigated this effect and its consequences for the emergent profiles, the so-called gravity darkening. As it turned out, the distortion of the stellar surface can be neglected for the line formation process and rotational rates lower than 300 km s^{-1}(for supergiants) and 400 km s^{-1} (for dwarfs). Although the modification of the photospheric parameters can be significant even for rotational velocities below these values, by defining appropriate *averaged* stellar parameters we obtained "effective" photospheric profiles that are independent of latitude, and which represent the actual behaviour extremely well. The photospheric parameters derived by standard 1-D methods represent these averaged values, almost independent of inclination angle, at least in the O-star case (cf. the discussion in §5.1). However, in order to determine the actual parameters (in particular, the stellar mass), one has to re-transform the derived averaged values by accounting for the rotational speed (or at least a guess of it, see below). Consequently it is possible to include gravity darkening in the usual procedure, which uses one set of stellar parameters that are independent of stellar latitude, provided that the modified definitions of stellar parameters like $\log g$ and $T_{\rm eff}$ are kept in mind.

In the first part of our analysis of line formation, we concentrated on the purely kinematical effects of stellar rotation, leaving the density at its 1-D value. Most importantly, we found the *resonance zone effect* to be responsible for modifying the line shape significantly: Because of the twisted resonance zones due to the *differential* rotation, the emission near the line core is diminished compared with the non-rotating case, while the wings develop emission humps, even though no quasi-disk is present. In this simplified model, the *equivalent width* of the profiles is the same as for the non-rotating case and the profile *shape* depends only on the projected rotational velocity $v_{\rm rot} \sin i$ and not on the absolute value of $v_{\rm rot}$.

In contrast, by accounting also for the modified 2-D density structure, the emergent profiles become dependent on both $v_{\rm rot}$ and $\sin i$, since the emitted line flux is – via the ρ^2-*effect*, a strongly non-linear function of density contrast (depending on $v_{\rm rot}$) and direction. In any case, however, the (re-defined) equivalent widths of the consistent profiles are *always* larger than those of the conventional 1-D profiles, and increase with increasing $v_{\rm rot}$ and decreasing $\sin i$.

For $v_{\rm rot} \lesssim 100$ km s^{-1} and/or $\dot{M} \lesssim 1 \cdot 10^{-6} M_\odot {\rm yr}^{-1}$ the differences (as function of $\sin i$ and compared with the 1-D approach) are generally small. In contrast the effects are significant for cases with a larger $v_{\rm rot}$ and substantial wind density. The largest discrepancies will always arise if the star is observed pole-on, when the projected area of the compression zone is a maximum.

If we compare the profiles for constant $v_{\rm rot} \sin i$ as function of $v_{\rm rot}$ (or compatible $\sin i$, respectively), the largest deviations turn out to be present for low values of $v_{\rm rot} \sin i$ *when the star is observed pole on*, since then the effects of high $v_{\rm rot}$ and maximum emitting area reinforce each other. For larger observed values of $v_{\rm rot} \sin i$, it is most probable that we observe the star equator on, where the ρ^2-effect is less effective due to the larger contributing volume of rarefied material.

Stellar rotation affects not only the equivalent width, but also the shape of H_α. We found that the line wings ($|X| \gtrsim 0.15$, in particular their slope) are affected mostly by $v_{\rm rot}$ alone, since the resonance zone effect and the differential ρ^2-effect (i.e., as function of inclination angle) roughly compensate each other. Hence, for a given $\dot{M}$, the line wings should be a good indicator of the absolute rotational rate. However, since the wings react significantly only for rotational rates $\gtrsim 200$ km s^{-1} and the influence of the steepness of the radial velocity field (i.e., β) also has to be accounted for, the diagnostic potential of the line wings must await further detailed investigation.

In contrast to the line wings, the central regions of the profiles ($|X| \lesssim 0.15$) are markedly affected by the inclination angle under which the star is observed. Due to the resonance zone effect, the profiles develop a double peaked structure. For intermediate wind densities, these show up as emission humps blue- and redwards from a central absorption component, which is much narrower than would be obtained from the 1-D case if convolved with the photospheric value of $v_{\rm rot} \sin i$. This theoretical prediction can actually be seen in a number of rapidly rotating stars, where, in order to fit the observed profile, the applied value of $v_{\rm rot} \sin i$ has to be decreased significantly below the one derived from photospheric lines (cf. Pu95). Additionally, the predicted emission humps may have their observational counterpart in the H_α profile of the rapid rotator ξ Per, as discussed in § 5.3.2. In this connection, we also note that the double-peaked morphology illustrated in Fig. 12 for large values of i and even for relatively modest rotational rates (~ 100 km s^{-1}) closely resembles the shape of the He II 4686 emission feature in Supergiants like ζ Pup and λ Cep. Thus, we speculate that the shapes of these He II wind features – which are not presently understood – might also be due to the effect of rotation on the structure of the stellar wind.

Although we did not attempt to perfom detailed line fits in this paper, the scaling relation for the equivalent width as function of $\dot{M}$ allowed us to derive estimates for the error introduced by using the conventional 1-D method for determining the mass-loss rate from H_α. We found maximum errors in the range between 50 . . . 70 %, again in the case for low $v_{\rm rot} \sin i$ when the star is observed pole on, whereas the typical error for the expectation value of $v_{\rm rot}$ is on the order of 20 . . . 30 %. Although this seems to be a fairly small number compared to the additional influences such as the slope of radial velocity field and possible clumping, two points have to be stressed: The influence of rotation is not an effect which will average out with a large enough number of observations but is a *systematic* effect, since – for given $\dot{M}$ – the 2-D equivalent width is always larger than in the 1-D treatment. Secondly, the *maximum* error is significant and moreover occurs in cases with low $v_{\rm rot} \sin i$, i.e., in cases where one is inclined to neglect rotation and where the profile *shape* hardly differs from the 1-D result (cf. Fig. 17). This may introduce large deviations for single objects from mean relations such as the WLR and wrong conclusions when observationally deduced and theroretically predicted mass-loss rates are compared.

Thus, a careful reanalysis of observed mass-loss rates that accounts for the effects of stellar rotation correctly is required. The major problem here is, of course, the determination of either $\sin i$ or $v_{\rm rot}$. This may be possible in certain cases, e.g., for the rapid rotator HD 93521, which has wind-compressed disk signatures in profiles of its UV resonance lines that indicate $i \sim 90°$ (Howarth & Reid, 1993; Bjorkman et al. 1994; Massa 1995), or in cases where the line shape is definitely influenced by rotation (as for ξ Per). In general, however, one will have to analyze also other spectral regions which behave differently with rotation. For this purpose, the investigation of the IR/radio continuum as indicated in the introduction or the analysis of IR-lines such as Br_α (e.g., Käufl 1993) may provide new and complementary insights. In both cases, the radiation originates in a larger volume compared to H_α, where in the outer wind part the equatorial density concentration has its maximum, and (for lines) the resonance effect plays no role since the velocity field is almost purely radial.

Before this comparison can be attempted, however, we have to improve our approach in order to deduce *quantitative* results. A first step is to incorporate the HeII blend and then try to fit the observed line shapes for the sample of Pu95, especially the rapidly rotating stars. It will be interesting to investigate the extent to which the re-analyzed objects will influence the recently derived WLR for hot stars.

Finally, we have to improve also our hydrodynamical description, following the approach by Owocki et al. (1994). Here, the influence of the v_Θ terms on the line formation has again to be inspected. Since these models have lower boundaries at much smaller velocities, we will of course have to give up the Sobolev approximation and to perform an "exact integration".

Acknowledgements. We thank Dr. A. W. Fullerton for many helpful comments and carefully reading the manuscript. Many thanks also Dr. A. Herrero for providing us with his grid of plane-parallel NLTE model fluxes and to the anonymous referee for many useful comments and suggestions. This work was supported by the Deutsche Forschungsgemeinschaft under grant Pu−117/2−1.

A. Analytical expressions for Φ' and $\mathrm{d}\mu/\mathrm{d}\mu_0$

Equation (13) for the azimuthal angle Φ' in the orbital plane (cf. Fig. 1) can be derived by solving the differential equation we obtain from dividing the radial velocity component v'_r by the azimuthal one v'_Φ (both velocities defined in the inclined orbit):

$$\frac{\mathrm{d}x}{\mathrm{d}\Phi'} = x^2 \left[\frac{v_\infty(\Theta_0)}{\sin\Theta_0\, v_{\rm rot}}\right] \left(1-\frac{b}{x}\right)^\beta$$

(cf. BC, Eq. 16). Using the initial condition, $\Phi'(x_i \equiv 1) := 0$, this yields

$$\Phi' = \underbrace{\frac{1}{b(1-\beta)}\left\{\left(1-\frac{b}{x}\right)^{1-\beta} - (1-b)^{1-\beta}\right\}}_{\equiv C_0}$$

$$\times\ \frac{\sin\Theta_0 v_{\rm rot}}{\zeta v_{\rm esc}\,(1-\sin\Theta_0(v_{\rm rot}/v_{\rm crit}))^\gamma}, \qquad \text{(A1)}$$

which is Eq. (13). In the case of $\beta = 1$, we finally have to apply L'Hospitale's rule and find

$$C_0 = \frac{1}{b}(\ln(1-b/x) - \ln(1-b)). \qquad \text{(A2)}$$

Now we will derive the expression for $\mathrm{d}\mu/\mathrm{d}\mu_0$. Accounting for the transformation (BC, Eq. 19)

$$\cos\Theta = \cos\Theta_0 \cos\Phi'$$

and with $\mu = \cos\Theta$, we obtain the following differential equation:

$$\frac{\mathrm{d}\mu}{\mathrm{d}\mu_0} = \cos\Phi' + \frac{\cos^2\Theta_0}{\sin\Theta_0}\frac{\mathrm{d}\Phi'}{\mathrm{d}(\sin\Theta_0)}\sin\Phi'. \qquad \text{(A3)}$$

On the other side, a differentiation of Eq. (A1) for Φ' with respect to $\sin\Theta_0$ yields

$$\begin{aligned}\frac{\mathrm{d}\Phi'}{\mathrm{d}(\sin\Theta_0)} &= \frac{\Phi'}{\sin\Theta_0}\left[1+\gamma\frac{(v_{\rm rot}/v_{\rm crit})\sin\Theta_0}{1-\sin\Theta_0(v_{\rm rot}/v_{\rm crit})}\right] \\ &\quad + \frac{v_{\rm rot}\sin\Theta_0}{v_\infty(\Theta_0)}\frac{\mathrm{d}C_0}{\mathrm{d}\sin\Theta_0}, \end{aligned} \qquad \text{(A4)}$$

where in comparison to BC (their Eqs. 24/25) we find an additional term, since b depends on Θ_0. $\mathrm{d}\,C_0/\mathrm{d}\sin\Theta_0$ is given by

$$\frac{\mathrm{d}C_0}{\mathrm{d}\sin\Theta_0} = \frac{\mathrm{d}C_0}{\mathrm{d}\,b}\frac{\mathrm{d}\,b}{\mathrm{d}\sin\Theta_0},$$

with

$$\frac{\mathrm{d}\,b}{\mathrm{d}\sin\Theta_0} = \left(\frac{v_{\rm min}}{v_\infty(\Theta_0)}\right)^{1/\beta}\frac{(-\gamma)v_{\rm rot}}{\beta\,(1-\sin\Theta_0(v_{\rm rot}/v_{\rm crit}))\,v_{\rm crit}}$$

and

$$\frac{\mathrm{d}\,C_0}{\mathrm{d}\,b} = \begin{cases} \dfrac{(b/x)(\beta-1)(1-b/x)^{-\beta} - (1-b/x)^{1-\beta}}{b^2(1-\beta)} + \dfrac{b\,(1-\beta)(1-b)^{-\beta} + (1-b)^{1-\beta}}{b^2(1-\beta)} & \beta \neq 1 \\[2ex] \dfrac{-\,((b/x)(1-b/x)^{-1} - \ln(1-b/x))}{b^2} + \dfrac{b\,(1-b)^{-1} + \ln(1-b)}{b^2} & \beta = 1 \end{cases}$$

In the limit $\Theta_0 \rightarrow 0$ (i.e., at the pole), we have

$$\begin{aligned} \sin\Theta_0 &= 0 \quad & \cos\Theta_0 &= 1 \\ \Phi' &\approx 0 \quad & \sin\Phi' &\approx \Phi' \\ \sin\Phi' &= 0 \quad & \cos\Phi' &= 1, \end{aligned}$$

and using Eqs. (A1) and (A4)

$$\frac{\cos^2\Theta_0}{\sin\Theta_0}\sin\Phi^{'}\frac{d\Phi^{'}}{d(\sin\Theta_0)} \approx \frac{C_0 v_{\rm rot}}{\zeta v_{\rm esc}}\frac{d\Phi^{'}}{d(\sin\Theta_0)} \approx \left(\frac{C_0 v_{\rm rot}}{\zeta v_{\rm esc}}\right)^2$$

we find as result

$$\left.\frac{d\,\mu}{d\,\mu_0}\right|_{\Theta_0=0} = 1 + \left(\frac{C_0 v_{\rm rot}}{\zeta v_{\rm esc}}\right)^2.$$

References

Abbott, D. C., Bieging, J. H., Churchwell, E., 1981, ApJ 250, 645
Abbott, D. C., Telesco, C. M., Wolf, S. C., 1984, ApJ 279, 225
Barlow, M. J., Cohen, M., 1977, ApJ 213, 737
Becker, S. R., Butler, K., 1992, A&A 265, 647
Becker, S. R., Butler, K., 1995b, A&A 294, 215
Becker, S. R., Butler, K., 1995a, A&A 301, 187
Bieging, J. H., Abbott, D. C., Churchwell, E., 1989, ApJ 340, 518
Bjorkman, J. E., Cassinelli, J. P., 1993 (BC), ApJ 409, 429
Bjorkman, J. E., Ignace, R., Tripp, T. M., Cassinelli, J. P., 1994, ApJ 435, 416
Cassinelli, J.P., Ignace, R., Bjorkman, J.E., 1995, "Winds from rotating Wolf-Rayet stars: The wind-compressed zone model", in: IAU Symposium 163, Wolf-Rayet Stars: Binaries, Colliding Winds, Evolution, eds. K. A. van der Hucht and P. M. Williams, Kluwer, Dortrecht, p. 191
Castor, J. I., 1970, MNRAS 149, 111
Collins II, G. W., 1963, ApJ 138, 1134
Collins II, G. W., 1965, ApJ 142, 265
Cranmer, S. R., Owocki, S. P., 1995 (CO), ApJ 440, 308
Friend, D., Abbott, D. C., 1986 (FA), ApJ 311, 701
Gabler, R., Gabler, A., Kudritzki, R. P., Puls, J., Pauldrach, A. W. A., 1989, A&A 226, 162
Groenewegen, M. A. T., Lamers, H. J. G. L. M., 1989, A&AS 79, 359
Haser, S.M., Lennon, D. J., Kudritzki, R. P., Puls, J., Walborn, N.R., Bianchi, L., Hutchings, J.B., 1994, Space Sci. Rev. 66, 187
Herrero, A., Kudritzki, R. P., Vilchez, J. M., Kunze, D., Butler, K., Haser, S., 1992, A&A 261, 209
Howarth, I. D., Reid, A. U. W., 1993, A&A 279, 148
Howarth, I. D., Prinja, R., Massa, D., 1995, ApJ 452, L65
Hummel, W., 1992, Strahlungstransport in den Hüllen von Be-Sternen, Ph.D. Thesis, Ruhr-Universität Bochum
Käufl, H.U., 1993, A&A 272, 452
Kudritzki, R. P., Hummer, D. G., Pauldrach, A. W. A., Puls, J., Najarro , F., Imhoff, J., 1992, A&A 257, 655
Kudritzki, R.P., Lennon, D. J., Puls, J., 1995, "Quantitative Spectroscopy of Luminous Blue Stars in Distant Galaxies". In: ESO Astrophysics Symposia, Science with the VLT, eds. J.R. Walsh and I.J. Danziger, Springer, Heidelberg, p. 246
Lamers, H. J. G. L. M., 1981, ApJ 245, 593
Lamers, H. J. G. L. M., Waters, L. B. F. M., 1984, A&AS 136, 37
Lamers, H. J. G. L. M., Waters, L. B. F. M., 1984a, A&AS 138, 25
Lamers, H. J. G. L. M., Leitherer C., 1993 (LL93), ApJ 412, 771
Leitherer, C., 1988a, ApJ 326, 356
Leitherer, C., 1988b, ApJ 334, 626
Leitherer, C., Robert, C., 1991, ApJ 377, 629
Massa, D., 1995, ApJ 438, 376
Mazzali, P. A., 1990, A&A 238, 191
McCarthy, J. K., Lennon, D. J., Venn, K. A., Kudritzki, R. P., Puls, J., and Najarro, F., 1995, subm. to ApJ
Owocki, S. P., Cranmer, S. R., Blondin, J. M., 1994, ApJ 424, 887
Owocki, S.P., 1994, ApSS 221, 3
Panagia, N., Felli, M., 1975, A&A 39, 1
Pauldrach, A. W. A., Puls, J., Kudritzki, R. P., 1986 (PPK), A&A 164, 86
Pauldrach, A. W. A., Kudritzki, R. P., Puls, J., Butler, K., Hunsinger, J., 1994, A&A 283, 525
Puls, J., Pauldrach, A. W. A., Kudritzki, R. P., Owocki, S. P., Najarro, F., 1993, in: Reviews in Modern Astronomy 6, ed. G. Klare, (Springer, Heidelberg), p. 271
Puls, J., Kudritzki, R. P., Herrero, A., Pauldrach, A. W. A., Haser, S. M., Lennon, D. J., Gabler, R., Voels, S. A., Vilchez, J. M., Wachter, S., Feldmeier, A., 1995 (Pu95), A&A (in press)
Rybicki, G. B., Hummer, D. G., 1978, ApJ 219, 654
Schaerer, D., Schmutz, W., 1994, A&A 288, 231
Scuderi, S., Bonanno, G., Di Benedetto, R., Spadaro, D., Panagia, N., 1992, ApJ 392, 201
Shlosman, I., Vitello, P., 1993, ApJ 409, 372
Sobolev, V., 1957, Soviet Astron., 1, 678
Stahl, O., Aab, O., Smolinski, J., and Wolf, B., 1991, A&A 252, 693
Wright, A. E., Barlow, M. J., 1975, MNRAS 170, 41

This article was processed by the author using Springer-Verlag LaTeX A&A style file *L-AA* version 3.